Cell Reports
Medicine

Article

Targeting PDGF signaling of cancer-associated fibroblasts blocks feedback activation of HIF-1α and tumor progression of clear cell ovarian cancer

Graphical abstract

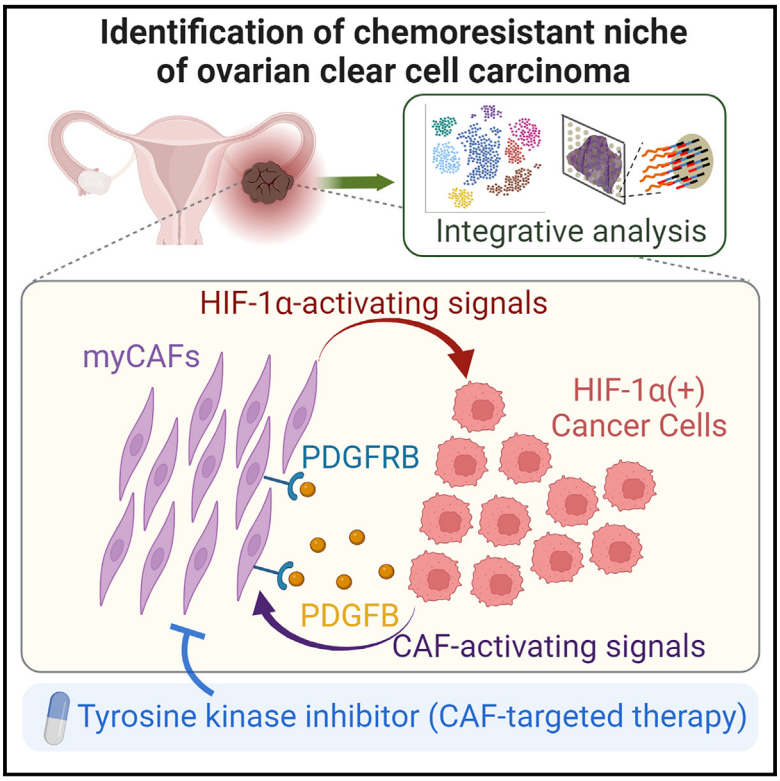

Highlights

- HIF-1α-positive cancer cells and CAFs form chemoresistant niches of OCCC
- PDGF from HIF-1α-positive cancer cells activates CAFs
- Activated CAFs induce HIF-1α expression and chemoresistance in cancer cells
- Inhibition of PDGF signaling in CAFs augments chemosensitivity of cancer cells

Authors

Yutaro Mori, Yoshie Okimoto, Hiroaki Sakai, ..., Kosuke Yoshihara, Takayuki Enomoto, Koji Okamoto

Correspondence

okamoto.kouji.dm@teikyo-u.ac.jp

In brief

Through an integration of spatial analyses and co-culture studies, Mori et al. demonstrate that feedback activation between HIF-1α-positive cancer cells and cancer-associated fibroblasts (CAF) contributes to chemoresistance of ovarian clear cell carcinoma. Targeted inhibition of CAF activation by a receptor tyrosine kinase inhibitor augmented chemosensitivity, suggesting possible application for CAF-targeted therapy.

Mori et al., 2024, Cell Reports Medicine 5, 101532
May 21, 2024
https://doi.org/10.1016/j.xcrm.2024.101532

CellPress

Cell Reports Medicine

CellPress
OPEN ACCESS

Article

Targeting PDGF signaling of cancer-associated fibroblasts blocks feedback activation of HIF-1α and tumor progression of clear cell ovarian cancer

Yutaro Mori,[1,5] Yoshie Okimoto,[1] Hiroaki Sakai,[1] Yusuke Kanda,[1] Hirokazu Ohata,[1] Daisuke Shiokawa,[2] Mikiko Suzuki,[3] Hiroshi Yoshida,[4] Haruka Ueda,[5] Tomoyuki Sekizuka,[5] Ryo Tamura,[5] Kaoru Yamawaki,[5] Tatsuya Ishiguro,[5] Raul Nicolas Mateos,[6] Yuichi Shiraishi,[6] Yasushi Yatabe,[4] Akinobu Hamada,[3] Kosuke Yoshihara,[5] Takayuki Enomoto,[5] and Koji Okamoto[1,7,*]

[1]Advanced Comprehensive Research Organization, Teikyo University, Tokyo 173-0003, Japan
[2]Ehime University Hospital Translational Research Center, Shitsukawa, Toon, Ehime 791-0295, Japan
[3]Division of Molecular Pharmacology, National Cancer Center Research Institute, Tokyo 104-0045, Japan
[4]Department of Diagnostic Pathology, National Cancer Center Hospital, Tokyo 104-0045, Japan
[5]Department of Obstetrics and Gynecology, Niigata University Graduate School of Medical and Dental Sciences, Niigata 951-8520, Japan
[6]Division of Genome Analysis Platform Development, National Cancer Center Research Institute, Tokyo 104-0045, Japan
[7]Lead contact
*Correspondence: okamoto.kouji.dm@teikyo-u.ac.jp
https://doi.org/10.1016/j.xcrm.2024.101532

SUMMARY

Ovarian clear cell carcinoma (OCCC) is a gynecological cancer with a dismal prognosis; however, the mechanism underlying OCCC chemoresistance is not well understood. To explore the intracellular networks associated with the chemoresistance, we analyze surgical specimens by performing integrative analyses that combine single-cell analyses and spatial transcriptomics. We find that a chemoresistant OCCC subpopulation with elevated HIF activity localizes mainly in areas populated by cancer-associated fibroblasts (CAFs) with a myofibroblastic phenotype, which is corroborated by quantitative immunostaining. CAF-enhanced chemoresistance and HIF-1α induction are recapitulated in co-culture assays, which show that cancer-derived platelet-derived growth factor (PDGF) contributes to the chemoresistance and HIF-1α induction via PDGF receptor signaling in CAFs. Ripretinib is identified as an effective receptor tyrosine kinase inhibitor against CAF survival. In the co-culture system and xenograft tumors, ripretinib prevents CAF survival and suppresses OCCC proliferation in the presence of carboplatin, indicating that combination of conventional chemotherapy and CAF-targeted agents is effective against OCCC.

INTRODUCTION

Although molecular-targeted and immune-based therapies have made a substantial impact on refractory cancers, many tumors eventually acquire chemoresistance. Such resistance can be attributed to intratumor cell-cell networks, which enable cancer cells to survive and proliferate after therapy.[1] Notably, cancer cells gain chemoresistance by forming cellular networks with non-tumor cells, such as cancer-associated fibroblasts (CAFs).[2,3] Therefore, to understand the biological basis of resistance, it is important to gain a global picture of intratumor heterogeneity and the cell-cell networks by which resistant cancer cells survive.

While both genetic and epigenetic alterations contribute to tumor heterogeneity, gene expression analyses in a variety of clinical tumors at the single-cell level have led to marked progress in understanding the epigenetic heterogeneity of clinical tumors.[4,5] Transcriptome analyses using single-cell RNA sequencing (scRNA-seq) or single-nucleus RNA-seq (snRNA-seq) have revealed the cellular composition of clinical tumors and the gene expression profiles of each population.[6] In addition, recent progress in spatial transcriptomics and other spatial omics approaches has enabled researchers to visualize gene expression in histological specimens and to stratify histological regions based upon these expression profiles.[7–9] In particular, integrative analyses of spatial transcriptomics using single-cell analysis has allowed the location of identified subpopulations to be visualized within tissue samples.[10]

Epithelial ovarian cancer (EOC) is a major gynecological malignancy.[11] Among the major subtypes of EOC, ovarian clear cell carcinoma (OCCC) at advanced stages is associated with a poor prognosis, which is mainly attributed to chemoresistance to standard regimens that include paclitaxel and carboplatin.[12,13] While alternative treatments for OCCC, such as immune checkpoint inhibitors or molecular targeted therapy against receptor tyrosine kinases, are in clinical trials, no effective alternative to standard chemotherapy has been developed.[14] Therefore, to develop an effective therapy for advanced OCCC is

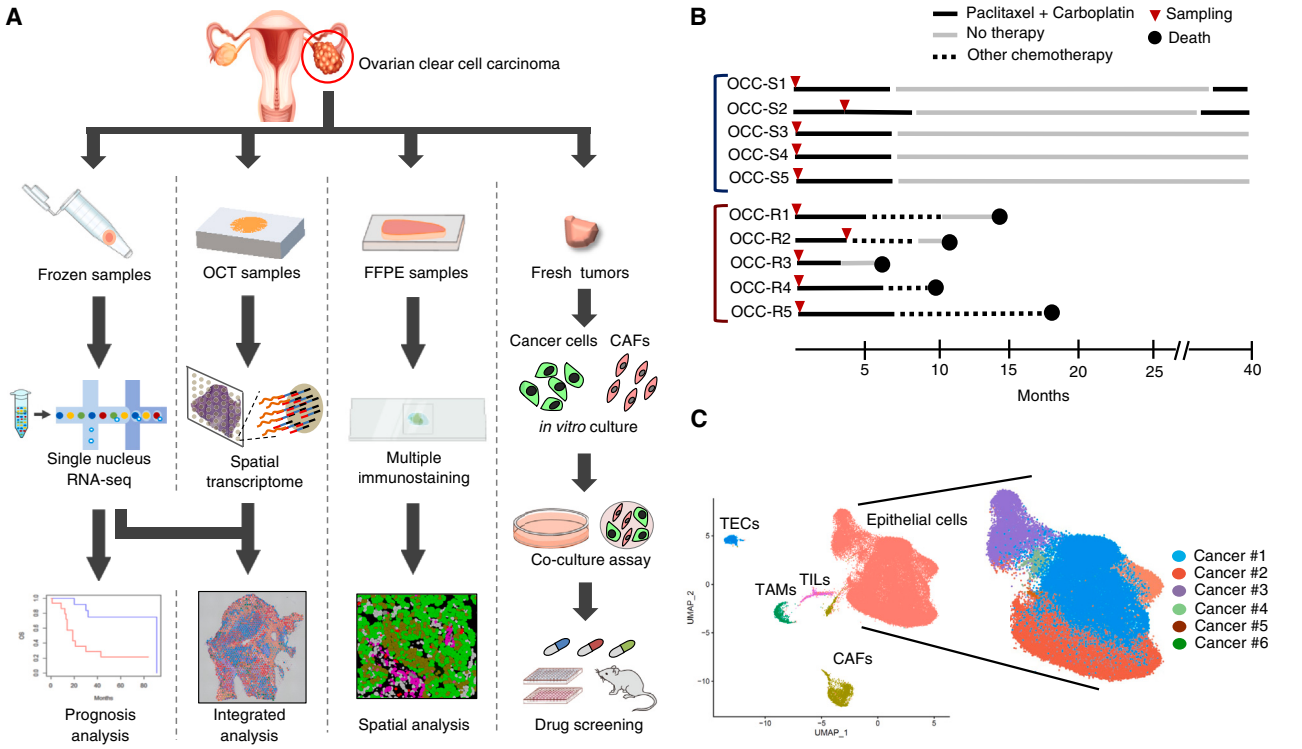

(legend on next page)

one of the major unmet medical needs in the field of gynecological oncology.

Previous studies examined the cellular heterogeneity of high-grade serous ovarian cancer (HGSOC), a major subtype of EOC, by performing scRNA-seq of patient ascites and found extensive inter-patient variability both in the tumor and non-tumor populations.[15] In another report, clinical specimens of HGSOC were examined by spatial transcriptomics to assess differences in spatial composition between poor responders and excellent responders to adjuvant chemotherapy.[16] Despite these pioneering studies, the cellular networks that define chemoresistance of HGSOC remain unclear, and no integrative studies of EOC, including OCCC, have been reported.

In this paper, to elucidate the cell-cell networks responsible for chemoresistance of OCCC, we performed integrative analyses of surgical specimens by combining snRNA-seq and spatial transcriptomics. By comparing results from chemosensitive and chemoresistant cases of OCCC, we identified a chemoresistant subpopulation that was localized in CAF-populated areas and associated with HIF-1α activation. Further investigations combining quantitative analyses of immunostaining, *in vitro* co-culture studies, and tumor xenograft models suggested that a feedback activation loop between HIF-1α-activated cancer cells and platelet-derived growth factor (PDGF)-activated CAF is the biological basis of OCCC chemoresistance. Furthermore, we demonstrated that inhibition of PDGF-mediated CAF activation, in combination with carboplatin, blocks OCCC proliferation, indicating effectiveness of CAF-targeting therapy for refractory cancers.

RESULTS

Identification of a cancer cell subpopulation associated with chemoresistance of OCCC

To identify intratumor networks responsible for chemoresistance of OCCC, we obtained frozen samples from surgical specimens and performed integrative analyses that combine single-cell analyses and spatial transcriptomics; subsequently, we extended the analyses by multicolor quantitative immunostaining, *in vitro* co-cultures, and mouse xenograft experiments (Figure 1A).

To obtain single-cell transcriptome data from frozen samples, we performed snRNA-seq[6] of chemosensitive (n = 5, OCC-S1–5) and chemoresistant (n = 5, OCC-R1–5) cases (Figure 1B; Table S1). The snRNA-seq data were then subjected to dimensionality reduction using uniform manifold approximation and projection (UMAP). Clustering of single-nucleus data presented on UMAP indicated that cells were stratified mainly according to clinical case, which was presumably caused by batch effects (Figure S1A). To eliminate batch effects and integrate individual datasets, we performed an anchoring procedure so that we could compare cell identity across samples[18] (Figure S1B).

After anchoring the data, we found that major cell types (epithelial cancer cells, CAFs, endothelial cells, and immune cells) formed distinct clusters upon UMAP presentation (Figures 1C, S1C, and S1D). Cells from both chemoresistant and chemosensitive cases were distributed within each cell type (Figure S1E). In the *EpCAM*$^+$ epithelial population, non-tumor cells were barely detectable based on an estimation of copy number alterations by InferCNV analyses[19] (Figure S1F), which was presumably attributed to careful elimination of non-tumor tissues during sample preparation.

To examine potential links between chemoresistance and oncogenic activations, we evaluated genomic alterations in major oncogenes and tumor suppressor genes using the NCC Oncopanel (Figure S1G). As reported previously, mutation of *ARID1A* and *PIK3CA* was identified in a large proportion of the samples (7 of 10 and 4 of 10 cases, respectively). However, there was no clear association with chemoresistance because both of these mutations occurred in both chemosensitive and chemoresistant cases (Figure S1G).

Next, to examine whether a chemoresistant cancer subpopulation exists, we stratified the *EpCAM*$^+$ tumor population into six subpopulations (Cancer #1–6) (Figures 1C and 1D). Remarkably, we found that a fraction of the Cancer #2 subpopulation was higher in chemoresistant cases than in chemosensitive ones (Figures 1D and 1E). On the other hand, evaluation of non-tumor cell types revealed no significant difference in numbers between chemoresistant and chemosensitive cases (Figures 1F and 1G).

The chemoresistant population of OCCC is associated with HIF activation and a poor prognosis

To determine the gene expression profiles of each cancer subpopulation, we isolated preferentially expressed signature genes (Figure S2A; Table S2). Examination of signature gene expression in advanced OCCC cases (n = 30) indicated that the signature of the Cancer #2 subpopulation, but not that of other subpopulations, was associated with shortened progression-free or overall survival (Figure 2A), linking the chemoresistance-associated Cancer #2 subpopulation to a poor prognosis.

Figure 1. Identification of a cancer cell subpopulation associated with chemoresistance of OCCC

(A) Study design based on surgical specimens of OCCC.

(B) Timeline presentation of 10 patients whose tumors were used for snRNA-seq, spatial transcriptome, and immunostaining analyses.

(C) UMAP presentation of snRNA-seq data obtained from chemoresistant (OCC-R1-5) and chemosensitive (OCC-S1-5) OCCC. Original snRNA-seq data from the 10 tumors (Figure S1A) were subjected to anchoring prior to data integration. Subsequently, the identity of cells in each cluster was determined based upon expression of marker genes,[17] as shown in Figure S1C. TEC, tumor endothelial cells; CAF, cancer-associated fibroblast; TAM, tumor-associated macrophage; TIL, tumor-infiltrating lympohcyte. The epithelial tumor population was further classified into six subpopulations (Cancer #1–6), denoted by the indicated colors.

(D) Stacked bar graph displaying the distribution of each cancer cell subpopulation (Cancer #1–6) in each tumor (left) and the percentage of cancer cells (right).

(E) Boxplots showing the fraction of the indicated cancer subpopulations in the chemoresistant and chemosensitive tumors shown in (D). The horizontal bars within the boxes indicate the median value. The top and bottom bars of the box denote the 25th and 75th percentiles, respectively. ***$p < 0.001$; n.s., not significant.

(F) Stacked bar graph displaying the distribution of non-tumor cell populations within each tumor (left) and the percentage of non-tumor cells (right).

(G) Boxplots showing the fractions of the indicated non-tumor populations. *$p < 0.05$, **$p < 0.01$, ***$p < 0.001$. p values were determined by Student's t test.

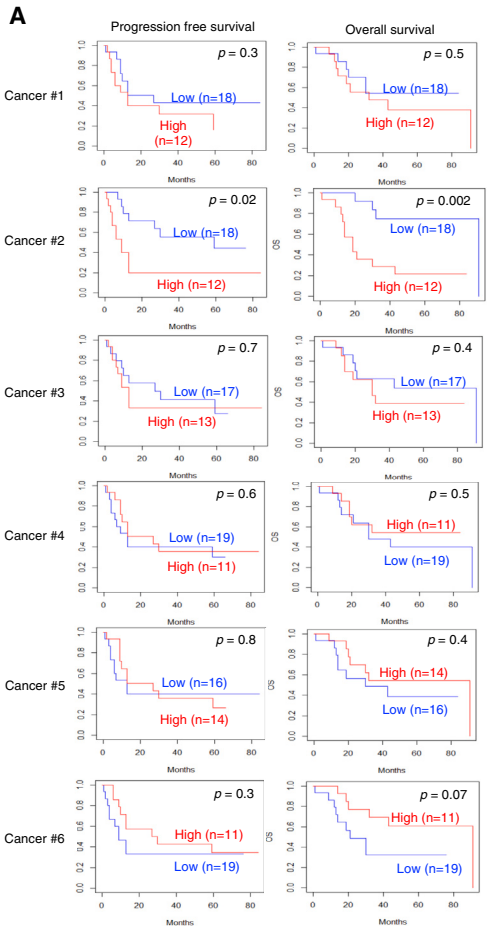

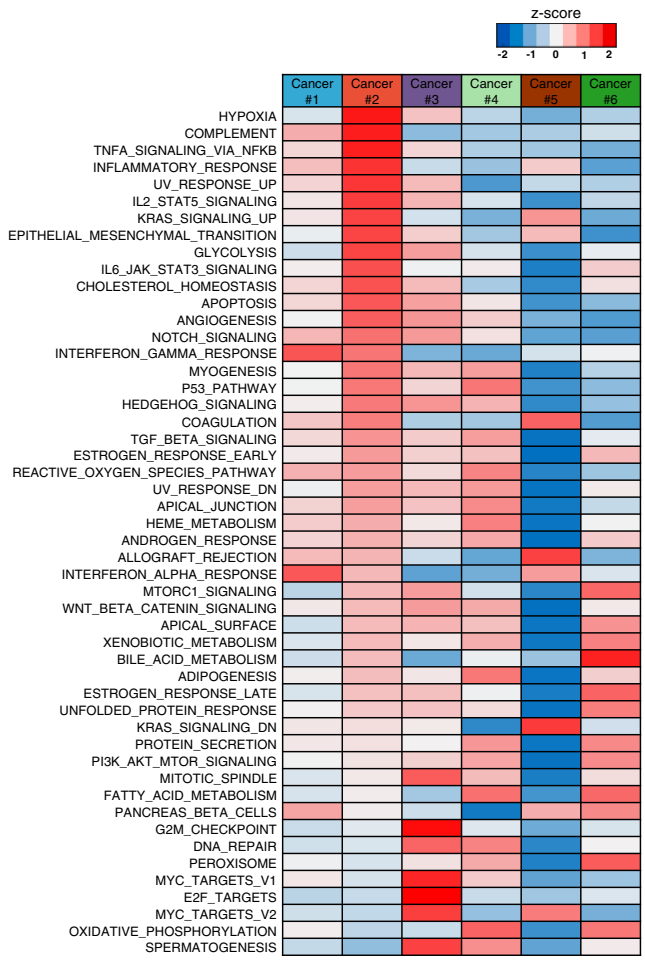

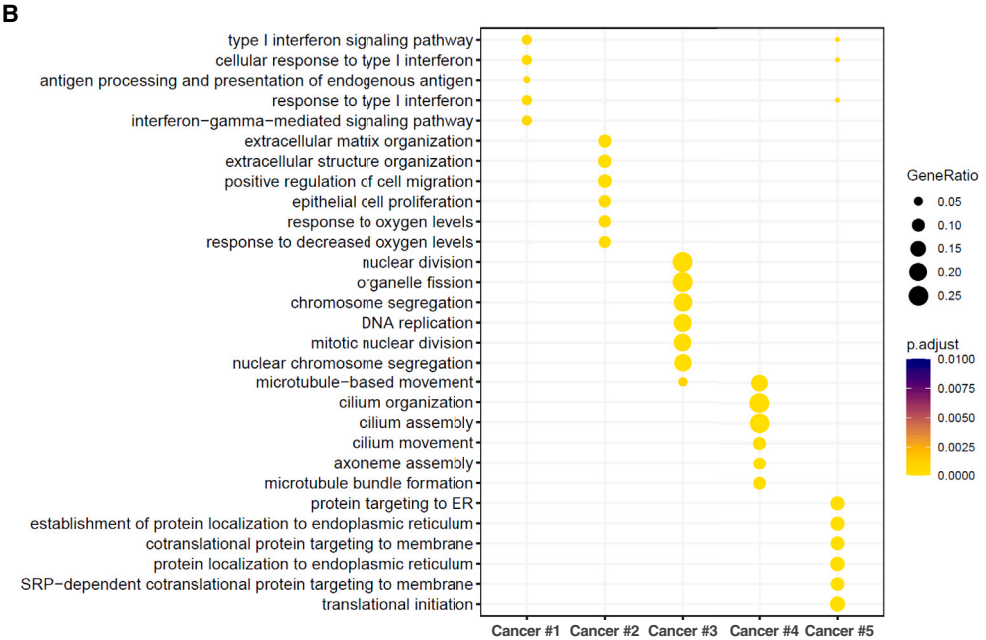

(legend on next page)

Next, we performed Gene Ontology (GO) enrichment analyses of the subpopulations to investigate their biological characteristics. The results showed that the Cancer #2 subpopulation was associated with hypoxic responses and with the extracellular matrix (Figure 2B). In accordance, single-sample gene set enrichment analyses (ssGSEA) of Hallmark signature gene sets revealed that hypoxia pathways were activated specifically in the Cancer #2 subpopulation (Figures 2C and S2B). On the other hand, enrichment analyses of the other major subpopulations indicated that the Cancer #1 and #3 subpopulations were associated with interferon response pathways and cell-cycle-related pathways (Figures 2B and 2C), respectively, suggesting that the Cancer #3 subpopulation is a cycling population.

Next, we performed virtual inference of protein activity by enriched regulon analysis to investigate transcriptional regulators associated with each cluster. In agreement with the findings of an elevated hypoxic response, the Cancer #2 subpopulation showed elevated activity of HIF1A (HIF-1α) and EPAS1 (HIF-2α) (Figures S2C and S2D). Of note, the top five transcription factors activated in the Cancer #2 subpopulation (HIF1A, EGR-1, ATF-2, EPAS1(HIF-2A), and SP-1) mediate hypoxic responses.[20] We found extensive overlap of target genes that were upregulated in the Cancer #2 subpopulation (Figure S2E), suggesting that these transcription factors co-operate to induce hypoxic responses. Taken together, these results indicate that the #2 chemoresistant subpopulation is associated with a poor prognosis and HIF-mediated hypoxic responses.

Chemoresistant cells are localized in CAF-populated areas of OCCC

Next, we attempted to determine the histological localization of the Cancer #2 chemoresistant cancer subpopulation by performing spatial transcriptomics analysis. Surgical specimens from chemoresistant (OCC-R2) and chemosensitive (OCC-S3) cases were subjected to Visium spatial gene expression analyses. Specific markers for epithelial cancer cells, CAFs, endothelial cells, and immune cells were used to determine the location of these cells within tumors. Hematoxylin and eosin (H&E) staining of serial sections indicated that the specimens were roughly segregated into cancer- or CAF-dominated regions (Figures 3A and S3A, far left). Consistent with this, we found that the tissue distribution of cancer cells and CAFs depicted by Visium analyses corresponded approximately to the cancer cell- or CAF-dominated regions visualized by H&E staining (Figures 3A and S3A). Indeed, Visium spots could be classified into three groups based upon gene expression profiles (Figures 3B and S3B): cancer-dominated, CAF-dominated, and cancer/CAF-mixed (Figures 3C and S3C). The distribution of the three types of spots corresponded approximately to that of cancer cells and CAFs observed in the H&E images (Figures 3D and S3D).

Next, to localize the major cancer subpopulations (#1–5), we performed anchor-based integration of snRNA-seq data and Visium data (STAR Methods) and then calculated a prediction score for each subpopulation in each Visium spot (Figures 3E and S3E). In both chemoresistant and chemosensitive cases, visualization of cancer subpopulations based upon the prediction scores revealed that the Cancer #2 subpopulation was localized mainly in cancer/CAF-mixed spots. By contrast, the Cancer #1 and #3 populations were localized mainly in cancer-dominated spots (Figures 3F and S3F).

In agreement with the snRNA-seq data, the Cancer #2 signature, but not the other signatures, was expressed to a greater extent in OCC-R2 than in OCC-S3 (Figure 3G), thereby supporting an association between cancer cells harboring the Cancer #2 signature and chemoresistance.

HIF-1α-induced cancer cells reside near CAFs in chemoresistant OCCC

Next, we immunostained HIF-1α-positive cancer cells to further investigate the location of the Cancer #2 chemoresistant populations in cancer/CAF-mixed areas. Remarkably, co-immunostaining of chemoresistant tumors (OCC-R1-5) with antibodies specific for HIF-1α, PAX8 (a marker for ovarian cancer cells), and α-SMA (a marker for CAFs) revealed widespread distribution of PAX8-positive cancer cells that co-express HIF-1α (Figure S4A). By contrast, the fraction of cancer cells co-expressing detectable HIF-1α in chemosensitive tumors (OCC-S1-5) was much lower than in chemoresistant tumors (Figure S4A). In fact, quantification of stained cells using QuPath (Figure S4B) indicated that the fraction of the HIF-1α-positive population in chemoresistant tumors was, on average, three times higher than that in the chemosensitive tumors (33.2% vs. 11.0%, respectively) (Figure S4C).

We observed that HIF-1α-positive cancer cells in chemoresistant tumors frequently localized near α-SMA-positive cells (Figures 3H and S4D). Indeed, evaluation of relative distance among HIF-1α-positive cancer cells, HIF-1α-negative cancer cells, and α-SMA-positive cells by nearest-neighbor analyses (CytoMAP) indicated the localization of HIF-1α-positive cancer cells near α-SMA-positive cells (Figures 3I and S4E). Accordingly, calculation of average distance from PAX8(+)/HIF-1α(+) cells or PAX8(+)/HIF-1α(−) cells to the nearest α-SMA(+) cells (QuPath) confirmed the localization of PAX8(+)/HIF-1α (+) cells near α-SMA(+) cells (Figures 3J and S4F). These data suggest that localization of HIF-1α-induced cancer cells near CAF is a hallmark of chemoresistant OCCC.

CAFs in chemoresistant tumors show a myofibroblastic phenotype

Close localization of CAFs to chemoresistant cells suggests that CAFs may play a functional role in enhancing the chemoresistance

Figure 2. A chemoresistant subpopulation of OCCC is associated with HIF activation and a poor prognosis

(A) Kaplan-Meier plots of advanced-stage OCCC (stages II–IV, $n = 30$). The top 20 genes highly expressed by each cancer subpopulation (Cancer #1–6) were selected as signature genes and used to classify the 30 cases of advanced OCCC (stages II–IV) into groups with high or low expression of signature genes. Kaplan-Meier curves show progression-free survival and overall survival in each group. p values were calculated using log rank test.

(B) Dot plot presentation of Gene Ontology (GO) terms specifically enriched in cancer subpopulations (Cancer #1–5).

(C) Heatmap of normalized ssGSEA enrichment scores for Hallmark pathways in cancer subpopulations (Cancer #1–6).

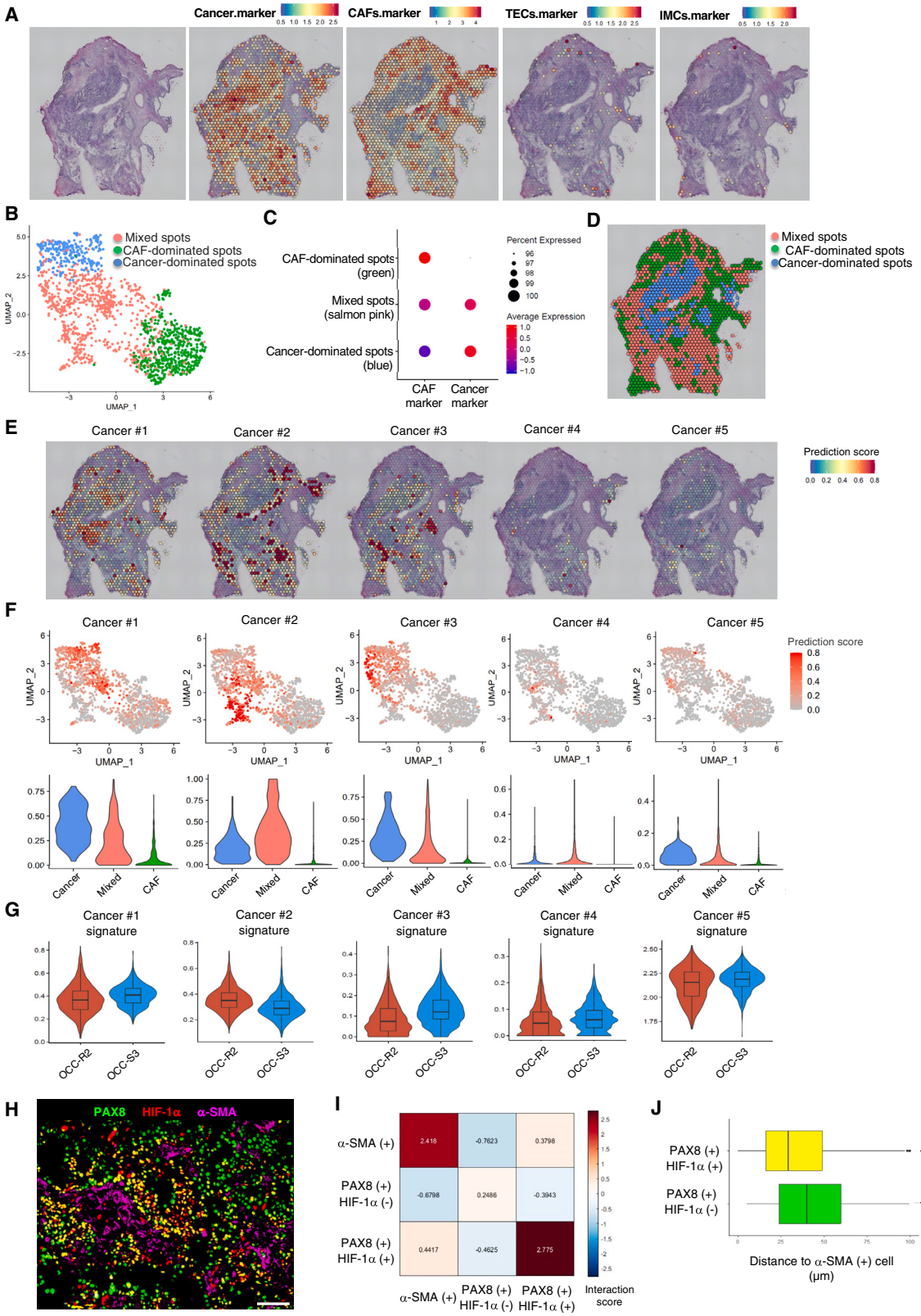

(legend on next page)

of OCCC. To examine a subpopulation of CAFs that may exist in chemoresistant OCCC, we used the snRNA-seq data to stratify the CAF population shown in Figure 1C. Contrary to stratification of the cancer population, however, we did not find a subpopulation that exists preferentially in chemoresistant OCCC (Figures 4A, S5A, and S5B).

As an alternative approach, we used the snRNA-seq data to examine whether CAFs from chemosensitive cancers were associated with any particular biological features. It has been reported that CAFs comprise heterogeneous populations, including inflammatory CAFs (iCAFs), antigen-presenting CAFs (apCAFs), and myofibroblastic CAFs (myCAFs), and that myCAFs reside close to cancer cells.[2,21] Comparison of CAFs from chemoresistant and chemosensitive tumors by ssGSEA and GO term analyses indicated that CAFs from chemoresistant OCCC were associated with epithelial-mesenchymal transition (EMT) and extracellular matrix organization (Figures 4B and 4C), phenotypes associated with myCAFs. Strikingly, CAFs from chemoresistant OCCC showed elevated expression of the myCAF gene signature (Figure 4D) and the myCAF-related genes *FAP*, *TPM1*, and *THBS2* (Figure 4E). In accordance, visualization of each CAF signature supported dominant distribution of myCAFs in chemoresistant but not in chemosensitive tumors (Figure S5C). Furthermore, immunostaining studies revealed higher levels of FAP-α (a protein encoded by the FAP gene) in chemoresistant tumors than in chemosensitive ones (Figure S5D). Collectively, these data indicate that the myCAF population is increased in chemoresistant cancer and that HIF-1α-induced OCCC cells and myCAFs constitute a cancer microenvironment associated with chemoresistant OCCC.

To establish the clinical importance of HIF1-α-positive cancer cells or FAP-α-expressing myCAFs in chemoresistant OCCC, we next examined their presence in a large set of formalin-fixed paraffin-embedded specimens of treatment-naive OCCC (86 cases: stage I, 45; stage II, 8; stage III, 24; stage IV, 9) by performing tyramide-based multicolor immunofluorescence for HIF-1α, PAX8, FAP-α, and α-SMA (Table S4; Figure S5E). To examine whether increased fractions of HIF-1α-positive cancer cells or FAP-α-expressing myCAFs affect the clinical course of OCCC, we calculated the fraction of HIF-1α-positive cells among PAX8-positive cancer cells and FAP-α-positive cells among α-SMA-positive CAFs. A fraction of HIF-1α-positive cancer cells were weakly associated with that of FAP-α-positive CAFs (Figure S5F), and we observed modest increases of fractions of these cells in advanced stages (Figure S5G). Of note, calculation of the relative distance from FAP-α-positive cells to the nearest HIF-1α-positive or HIF-1α-negative cancer cells (QuPath) indicated the localization of HIF-1α-positive cancer cells near FAP-α-positive cells (Figure S5H), suggesting localization of HIF-1α-induced cancer cells near active CAFs.

Remarkably, Kaplan-Meier analyses revealed that a higher fraction of these cells in tumors was associated with poor prognosis and that patients with both high fractions (>10%) of HIF-1α-positive cancer cells (HIF-1α^{high}) and high fractions (>80%) of FAP-α-positive CAFs (FAP-α ^{high}) suffered from significantly worse prognoses than the other groups (Figure 4F). In accordance, univariate analyses showed that fractions of HIF-1α- and FAP-α -positive cells were associated with progression-free and overall survival (Figure 4G). Furthermore, multivariate analyses indicated that both fractions were prognostic factors independent of advanced stages (Figure 4H). These data indicate that expansion of HIF-1α-positive cancer cells and myCAFs negatively affects the clinical courses of OCCC, presumably as a result of aggravated chemoresistance.

In vitro co-cultivation of CAFs with chemoresistant OCCC cells recapitulates the chemoresistant niche

Co-localization of the chemoresistant subpopulation of cancer cells and CAFs implies mutual crosstalk between these cells in chemoresistant niches. To examine potential crosstalk between these cells, we established an *in vitro* co-culture system. First, we established cancer spheroids and CAFs separately from fresh surgical OCCC specimens. Second, we retrospectively selected chemoresistant cancer-derived spheroids based upon extensive expression of HIF-1α in cancer cells in the original surgical specimens (data not shown). The identities of the selected cancer spheroids and CAFs were confirmed by expression of specific markers: PAX8 and KRT7 for OCCC and α-SMA

Figure 3. HIF-1α-positive chemoresistant cells reside near CAFs in chemoresistant OCCC

(A) Far left: H&E staining of OCC-R2 tissue sections. Right: Visium spatial transcriptomics (ST) spots on H&E-stained sections were overlaid with spatial feature plots of ovarian cancer cell markers (*EPCAM*, *PAX8*, and *KRT7*), CAF markers (*COL1A1*, *COL1A2*, *DCN*, and *VIM*), endothelial cell (TEC) markers (*VWF*, *CDH5*, and *PECAM1*), or an immune cell marker (*PTPRC*).

(B) UMAP plots of the Visium ST spots shown in (A). ST spots were classified into three clusters by unsupervised clustering and are denoted by different colors.

(C) Dot plots showing average expression of CAF markers and ovarian cancer cell markers by the indicated clusters. Three clusters shown in (B) were designated as cancer-dominated spots, CAF-dominated spots, and mixed spots, based upon expression of these markers.

(D) Spatial presentation of the three cluster in OCC-R2 tissue sections. Tissue localization of the clustered ST spots was visualized and is denoted by the indicated colors.

(E) Spatial feature plots of the prediction scores for the indicated cancer subpopulations (Cancer #1–5) in OCC-R2 tissue sections.

(F) Top: UMAP feature plots of ST spots of OCC-R2. Prediction scores for the indicated cancer subpopulations are shown in red. Bottom: violin plots of the prediction scores for the cancer subpopulations shown in the top columns. ST spots were classified into three groups as shown in (D), and the prediction scores for each group are presented.

(G) Violin plots showing the average expression values for the signature genes expressed by the indicated cancer subpopulations (Cancer #1–5) in ST spots of OCC-R2 and OCC-S3. In the boxplots inside the violin plots, the top and bottom bars of the boxes represent the 25th and 75th percentile, respectively, and the horizontal bars within the box indicate the median value.

(H) Representative magnified images of HIF-1α(+) cancer cells near α-SMA(+) CAFs in a chemoresistant tumor (OCC-R3). Scale bar, 100 μm.

(I) Nearest-neighbor analysis of the image shown in (H).

(J) Boxplot showing the average distance from PAX8(+)/HIF-1α(+) cells or PAX8(+)/HIF-1α(−) cells to the closest α-SMA(+) cell, calculated using the image shown in (H). ***$p < 0.001$. p values were determined by Student's t test.

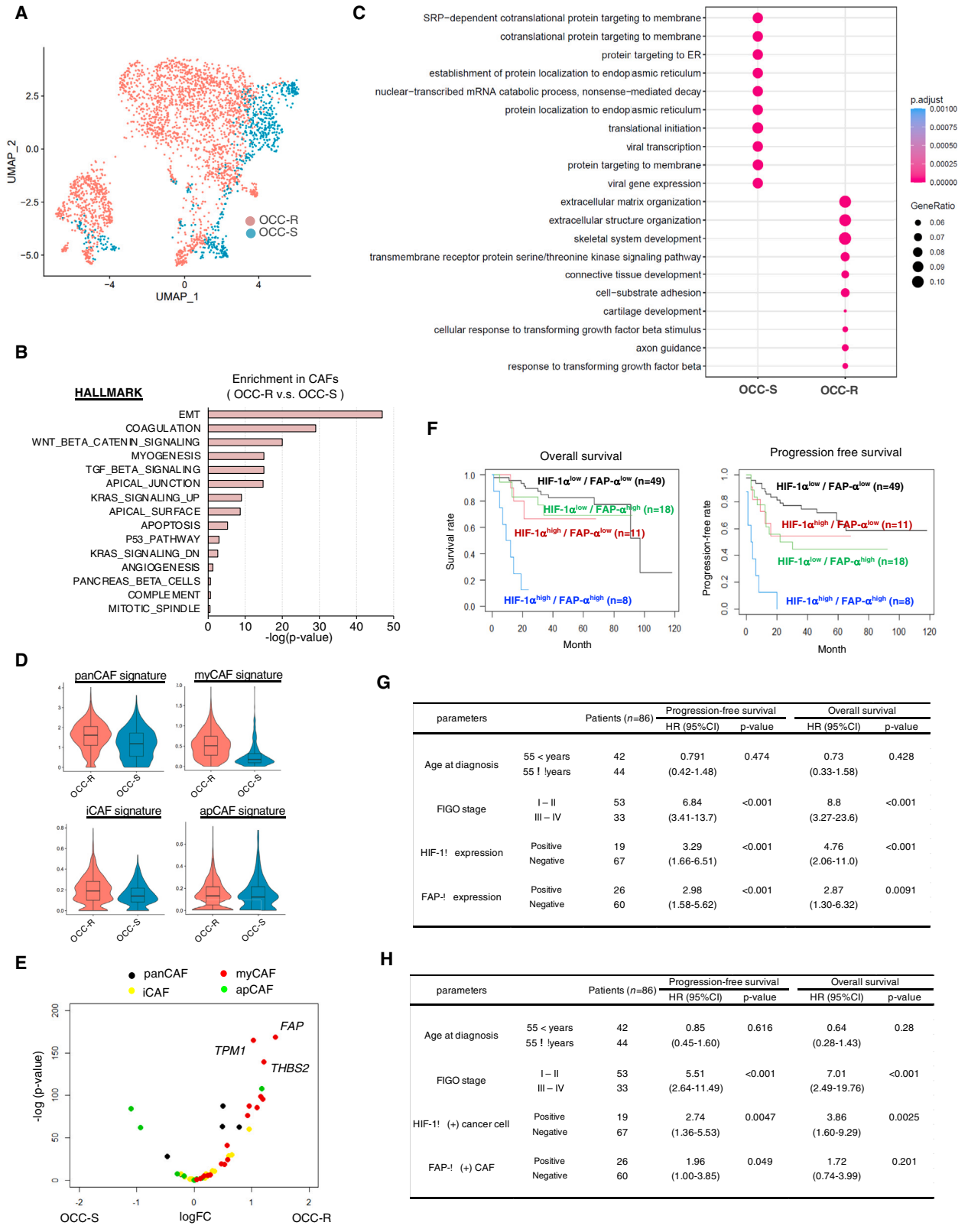

G

parameters		Patients (*n*=86)	Progression-free survival		Overall survival	
			HR (95%CI)	p-value	HR (95%CI)	p-value
Age at diagnosis	55 < years	42	0.791	0.474	0.73	0.428
	55 ! !years	44	(0.42-1.48)		(0.33-1.58)	
FIGO stage	I – II	53	6.84	<0.001	8.8	<0.001
	III – IV	33	(3.41-13.7)		(3.27-23.6)	
HIF-1! expression	Positive	19	3.29	<0.001	4.76	<0.001
	Negative	67	(1.66-6.51)		(2.06-11.0)	
FAP-! expression	Positive	26	2.98	<0.001	2.87	0.0091
	Negative	60	(1.58-5.62)		(1.30-6.32)	

H

parameters		Patients (*n*=86)	Progression-free survival		Overall survival	
			HR (95%CI)	p-value	HR (95%CI)	p-value
Age at diagnosis	55 < years	42	0.85	0.616	0.64	0.28
	55 ! !years	44	(0.45-1.60)		(0.28-1.43)	
FIGO stage	I – II	53	5.51	<0.001	7.01	<0.001
	III – IV	33	(2.64-11.49)		(2.49-19.76)	
HIF-1! (+) cancer cell	Positive	19	2.74	0.0047	3.86	0.0025
	Negative	67	(1.36-5.53)		(1.60-9.29)	
FAP-! (+) CAF	Positive	26	1.96	0.049	1.72	0.201
	Negative	60	(1.00-3.85)		(0.74-3.99)	

(legend on next page)

and collagen I for CAF (Figure S6A). Third, the spheroids and CAFs were labeled with GFP and mCherry, respectively, and then cultivated alone or together (at a 1:1 ratio) to examine cell proliferation and phenotypic alterations induced by co-cultivation (Figures 5A and 5B). Indeed, co-cultivation increased the survival rate of CAFs (Figure 5C) and induced expression of HIF-1α and HIF-2α in cancer spheroid cells (Figures 5D and 5E). Remarkably, co-culture increased chemoresistance to carboplatin (Figure 5F), indicating that the presence of CAFs contributes to chemoresistance of OCCC.

Next, to examine changes in gene expression induced after co-culture, we performed scRNA-seq of cells cultivated under monoculture or co-culture conditions (Figures 5G and S6B). When we compared the gene expression profiles of cancer spheroids under co-culture and monoculture conditions by ssGSEA, we found that four of five top Hallmark signatures (EMT, tumor necrosis factor alpha signaling via nuclear factor κB, inflammatory response, and hypoxia) induced after co-culture were identical to those upregulated in the Cancer #2 subpopulation (Figures 2C and S6C). In addition, co-culture with CAFs caused specific up-regulation of the Cancer #2 gene signature (Figure 5H, $p < 0.001$) and induced activation of all nine top transcription factors activated in the Cancer #2 subpopulation (Figures S2C and S6D). Collectively, phenotypic alteration of cancer spheroids induced by co-cultivation with CAFs largely simulated the gene expression profiles of the Cancer #2 subpopulation.

We also compared gene expression profiles of CAFs under co-culture and monoculture conditions by ssGSEA. The EMT pathway, which was strongly upregulated in CAFs in chemoresistant OCCC (Figure 4B), was induced under co-culture conditions (Figure S6E). In addition, we found that transforming growth factor β (TGF-β) signaling was strongly induced after co-cultivation (Figure S6E), suggesting that TGF-β signaling, which is a well-known signaling pathway that drives CAF generation,[2,23] may account for the EMT phenotype of the CAF induced under co-culture conditions. Furthermore, co-cultivation upregulated the myCAF signature (Figure 5I, $p < 0.001$) as well as genes representative of myCAF, including *FAP*, *THBS2*, and *TPM1* (Figure S6F), induction of which was also observed in chemoresistant OCCC (Figure 4E). Thus, both cancer spheroids and CAFs, when incubated together, undergo phenotypic alterations associated with chemoresistant OCCC. These data strongly suggest that interactions between cancer cells and CAFs lead to formation of a chemoresistant niche in OCCC.

CAF activation by cancer-derived PDGF mediates chemoresistance and activates HIF-1α in cancer cells

To better understand the molecular mechanism underlying chemoresistance mediated by the cancer-CAF interaction, we used NicheNet[24] to examine potential ligand-receptor interactions between these cells (Figure S7A). When we examined the snRNA-seq data, we identified 12 ligand-coding genes that were highly expressed in the Cancer #2 subpopulation (*NAMPT*, *EFNA5*, *PDGFB*, *C3*, *ANXA1*, *SPP1*, *FN1*, *ITGB1*, *LAMC2*, *LAMB1*, *LAMA1*, and *RELN*) (Figure S7A). Receptor-ligand analyses revealed that interaction between PDGFB (the β subunit of PDGF) and PDGFRB (the β subunit of PDGF receptor) was a strong candidate mediator of cell-cell signaling between cancer cells and CAFs (Figure S7A). In support of this, *PDGFB* was preferentially expressed in the Cancer #2 subpopulation from chemoresistant tumors (Figure S7B), and immunostaining of chemoresistant tumor showed activating phosphorylation of PDGFRB in α-SMA-positive CAFs that resided near KRT7-positive cancer cells (Figure S7C). Activation of CAF by PDGF signaling has also been reported in other types of cancer.[2,3]

Therefore, we next examined the functional significance of the PDGF-PDGFR interaction in the co-culture system. As expected, PDGFB and PDGFRB were expressed at high levels by cancer spheroid cells and CAFs, respectively (Figure 6A). Co-culture led to activating phosphorylation of PDGFR (p-PDGFRB) and expression of a myCAF marker (FAP-α) in CAFs (Figure 6B). Indeed, treatment of CAFs with a purified PDGFB ligand induced phosphorylation of PDGFRB and expression of FAP-α (Figure 6C) and increased proliferation of CAFs (Figure 6D), thereby phenocopying the effects of co-culture with cancer spheroids. Conversely, CRISPR-mediated knockout of PDGFRB in CAFs abolished PDGF-mediated proliferation (Figures 6E and 6F) and FAP-α expression (Figure 6G), indicating that the PDGFB-induced proliferation and expression of the myCAF-like phenotype were mediated by activation of the PDGF receptor in CAFs. In accordance, immunostaining of chemoresistant OCCC showed activating phosphorylation of PDGFRB in

Figure 4. CAFs in chemoresistant tumors are associated with myofibroblastic phenotype

(A) UMAP plot of CAFs, color-coded as chemoresistant (OCC-R1-5) or chemosensitive (OCC-S1-5) cases.

(B) Bar chart showing enrichment of specific biological pathways in CAFs from resistant tumors. Enrichment of a pathway is calculated by comparing the average ssGSEA values of Hallmark gene sets in CAFs from five chemoresistant and five chemosensitive tumors. *p* values for the top 15 Hallmark terms enriched in CAFs from chemoresistant cases were determined by Student's t test. $^{**}p < 0.01$.

(C) Dot plot of biological GO terms upregulated in CAFs from chemoresistant (OCC-R) and chemosensitive (OCC-S) cases.

(D) Violin plots of the signature scores for the indicated CAFs from chemoresistant and chemosensitive cases.

(E) Volcano plots showing preferential induction of myCAF signature genes in CAFs from chemoresistant cases. Average expression values for the indicated CAF signature genes[22] expressed by CAFs from chemoresistant and chemosensitive cases were calculated, and the relative ratios are shown. The horizontal and vertical axes represent the $\log_{10}$ values of fold changes and *p* values, respectively. Red dots, myCAF signature genes; yellow dots, iCAF signature genes; green dots: apCAF signature genes; black dots, panCAF signature genes. A list of the signature genes is presented in Table S3.

(F) Kaplan-Meier plots of OCCC (stages I–IV, $n = 86$). The patients were stratified into 4 groups: HIF-1α^{low}/FAP-α^{low} ($n = 49$), HIF-1α^{high}/FAP-α^{low} ($n = 11$), HIF-1α^{low}/FAP-α^{high} ($n = 18$), and HIF-1α^{high}/FAP-α^{high} ($n = 8$). Kaplan-Meier curves of progression-free survival and overall survival in each group are shown.

(G and H) Association of HIF-1α and FAP-α expression with poor prognosis. Association of the indicated parameters with progression-free survival or overall survival was evaluated by univariate (G) and multivariate (H) analyses (86 cases of OCCC). Hazard ratios (HRs), 95% confidence intervals, and *p* values were calculated with Cox's proportional hazards regression model. $^{***}p < 0.001$.

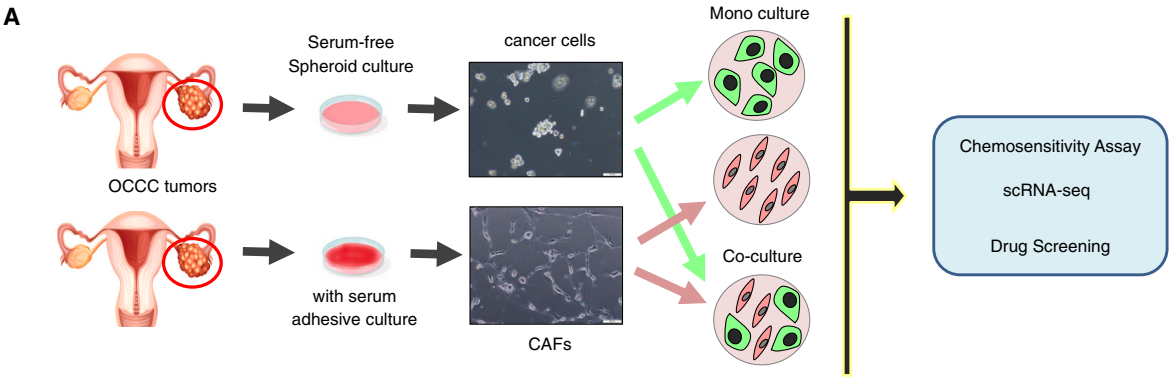

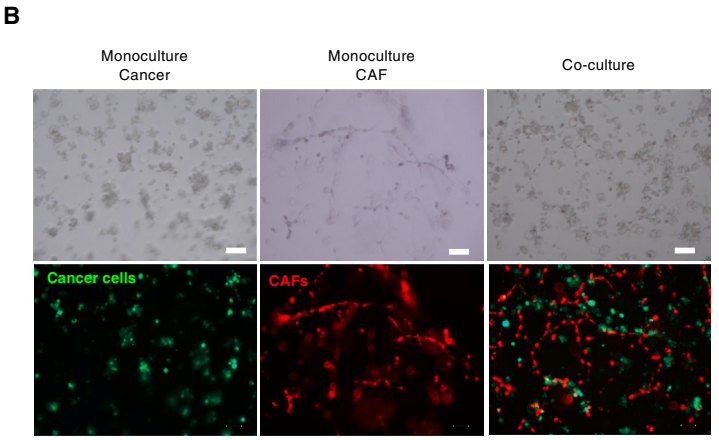

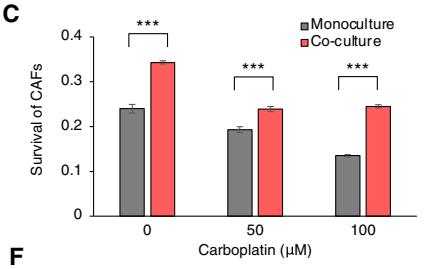

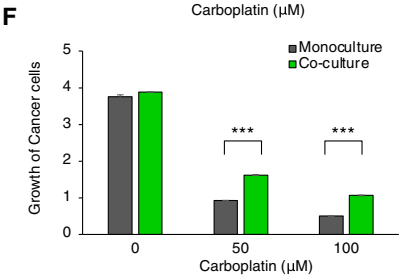

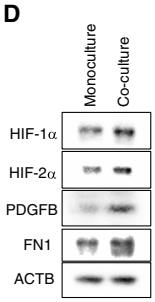

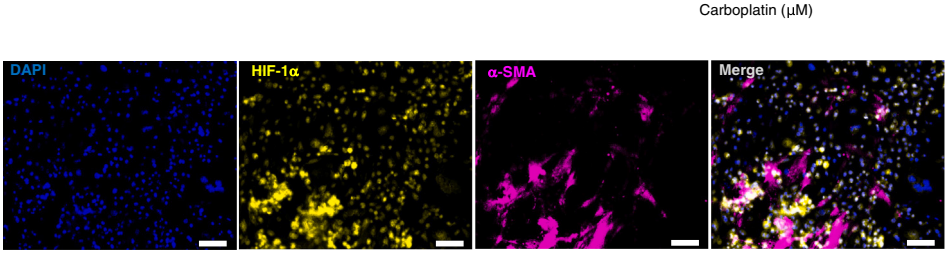

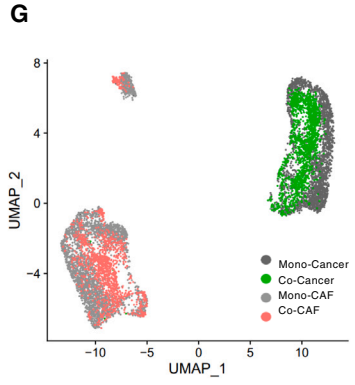

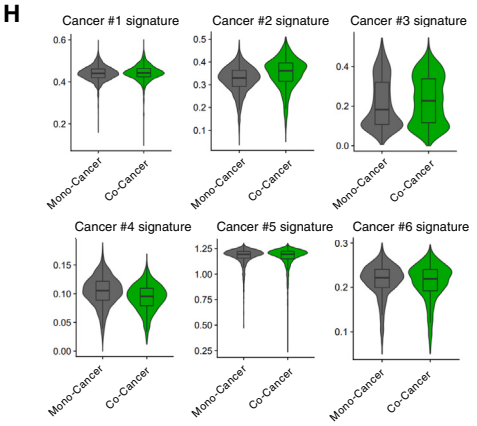

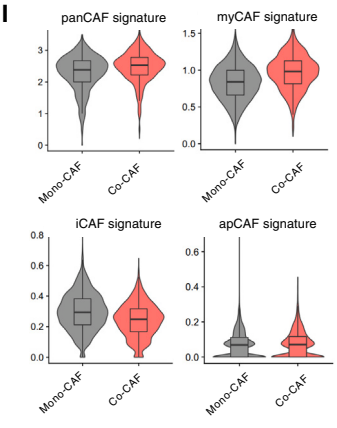

(legend on next page)

α-SMA-positive CAFs that resided near KRT7-positive cancer cells (Figure S7C).

Next, we examined the functional role of PDGFR signaling in cancer chemoresistance. *PDGFR* knockout in CAFs reduced its viability (Figure 6H). Remarkably, the *PDGFRB* knockout in CAFs inhibited expression of HIF-1α, HIF-2α, and PDGFB in cancer cells (Figure 6I). Moreover, the knockout reduced cancer chemoresistance to carboplatin (Figure 6J). Taken together, these data indicate the presence of a positive feedback loop between cancer cells and CAFs: PDGF expressed by OCCC induces PDGFR-mediated activation and survival of CAFs, which, in turn, augments HIF activation, PDGF expression, and chemoresistance in cancer cells.

CAF inhibition by ripretinib in combination with carboplatin inhibits growth of OCCC

The crucial role of the PDGF-PDGFR signaling axis in CAF-mediated chemoresistance tempted us to devise an effective therapy targeting PDGFR signaling in CAFs. To this end, we initially searched for tyrosine kinase inhibitors (TKIs) that inhibit CAFs. Carboplatin did not have any significant effect on CAF growth (Figure 7A). TKIs showed varying levels of growth inhibition, with ripretinib showing decent efficacy (Figures 7A and S8A). In fact, 1 μM ripretinib inhibited activating phosphorylation of PDGFRB and expression of FAP-α within 24 h (Figure S8B). Subsequently, we examined the inhibitory effects of ripretinib in the presence or absence of carboplatin in the *in vitro* co-culture system. As expected, ripretinib at 1–5 μM effectively reduced the viability of CAFs even in the absence of carboplatin (Figure 7B). Importantly, inhibition of cancer cell proliferation by carboplatin was markedly enhanced by ripretinib (Figures 7C and 7D). By contrast, ripretinib did not show significant enhancement of carboplatin-mediated inhibition upon monoculture of cancer cells (Figure 7E), indicating that ripretinib inhibits OCCC growth via CAF suppression.

Finally, we examined the effect of combined treatment with carboplatin and ripretinib on OCCC xenografts. The cancer spheroids and CAFs used in the co-culture assays were mixed at a 1:1 ratio and transplanted subcutaneously into immunocompromised NOG mice. Notably, ripretinib in combination with carboplatin led to marked inhibition of tumor growth (Figures 7F, S8C, and S8D).

According to our model, ripretinib inhibits growth of chemoresistant OCCC by inhibiting CAF. Therefore, we predicted that a fraction of the HIF-1α-positive cancer cells would be reduced in the presence of ripretinib. Indeed, we observed a marked reduction in a fraction of HIF-1α-positive cancer cells (Figures 7G and 7H) as well as α-SMA-positive CAFs (Figure S8E) after treatment.

We could generate xenografted tumors when only the cancer spheroids were used for the transplantation. We observed extensive infiltration of α-SMA-positive cells in the generated tumors (Figure S8F), suggesting that host-derived CAFs were also capable of interacting with xenografted cancer cells. Indeed, ripretinib enhanced the inhibition of tumor growth by carboplain (Figure S8G). Collectively, these data indicate that CAF inhibition is an effective treatment that eliminates chemoresistant OCCC when combined with standard chemotherapy agents.

DISCUSSION

Recent progress in spatial transcriptomics and other spatial omics technologies has enabled visualization of the molecular architecture of cancer tissues in histological samples.[7,9] The spatial location of cell populations of interest can be inferred by integrating spatial transcriptomics with single-cell gene expression analyses.[10,26,27] Here, we exploited the power of this integrative approach to determine the spatial localization of regions associated with OCCC chemoresistance. These studies, in combination with multicolor immunostaining, revealed that chemoresistance is associated with regions in which HIF-1α-activated cancer cells co-localize with myCAFs and that expansion of these cells profoundly affects the prognosis of OCCC patients.

Integrative analyses of snRNA-seq and the spatial transcriptome are descriptive in nature; therefore, we used an *in vitro* co-culture system to functionally validate the importance of interactions between cancer cells and CAFs. Previously, we established spheroid cultures from clinical specimens of HGSOC and colorectal cancer and investigated their biological characteristics.[28–31] By applying a similar method, we established spheroid cultures from surgical specimens of OCCC and showed that OCCC-derived CAFs confer chemoresistance

Figure 5. Co-cultivation of CAFs with chemoresistant OCCC cells recapitulates the chemoresistant niche *in vitro*

(A) Experimental design of the *in vitro* co-culture system. Cancer spheroid cells and CAFs were derived from surgical specimens of HIF-1α-positive OCCC. The established cancer cells and CAFs were labeled with GFP/Luc2 and mCherry/hRluc, respectively; cultivated either alone or in combination; and subjected to a chemosensitivity assay, scRNA-seq, or drug screening.

(B) Bright-phase images (top) and fluorescence images (bottom) of the indicated cells cultivated under organoid conditions for 7 days. Scale bars, 100 μm.

(C) Survival of CAFs upon monoculture or co-culture with cancer cells (OVN-48) for 7 days. Cultured cells were grown in the absence or presence of the indicated concentrations of carboplatin, and cell survival was evaluated by measuring hRLuc activity. The data are presented as mean ± SD (n = 3). p values were determined by Student's t test. ***$p < 0.001$.

(D) Western blot analyses of cancer cells that were sorted by fluorescence-activated cell sorting (FACS) after incubation under monoculture or co-culture conditions for 3 days.

(E) Representative image of immunostaining of HIF-1α and α-SMA in cancer cells and CAFs co-cultured for 3 days. Scale bars, 100 μm.

(F) Cancer cell growth (OVN-48) upon monoculture or co-culture with CAFs for 7 days. Cultured cells were grown in the absence or presence of the indicated concentrations of carboplatin, and cancer cell proliferation was evaluated by measuring Luc2 activity (n = 3). ***$p < 0.001$.

(G) UMAP plot of scRNA-seq data from cancer cells (OVN-48) and CAFs incubated under monoculture and co-culture conditions for 3 days.

(H) Violin plots of the signature scores for the cancer subpopulations (Cancer #1–6) grown under the monoculture and co-culture conditions in (G).

(I) Violin plots of the indicated signature genes in CAFs grown under the monoculture and co-culture conditions shown in (G). Statistically significant differences are indicated: ***$p < 0.001$.

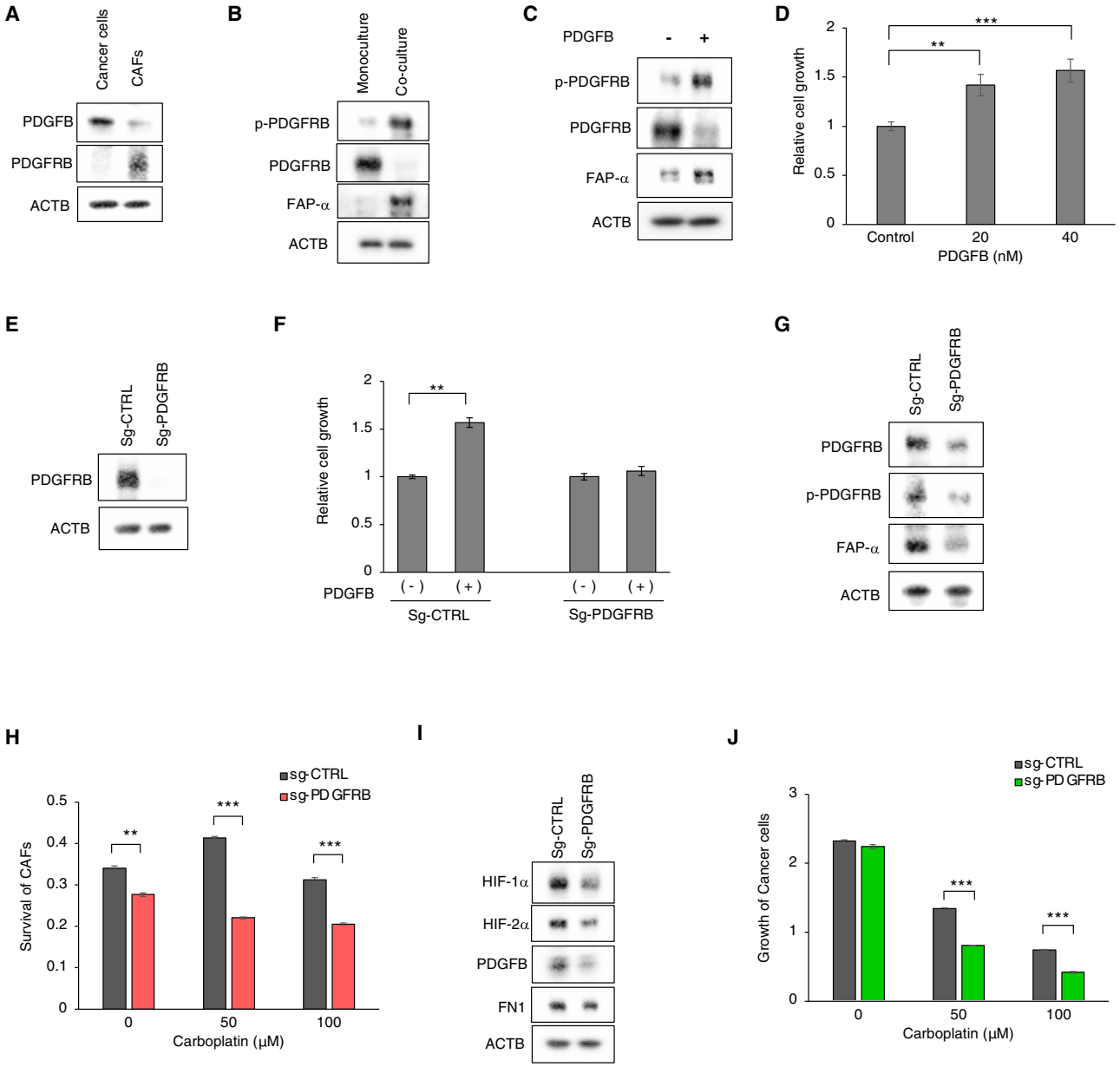

Figure 6. CAF activation by cancer-derived PDGF mediates chemoresistance and HIF-1α activation of cancer cells

(A) Western blot analysis of GFP-labeled cancer cells (OVN-48) and mCherry-labeled CAFs with the indicated antibodies.

(B) Western blot analysis of CAFs, grown under monoculture or co-culture conditions for 3 days with the indicated antibodies. Note that a PDGFRB level was reduced under co-culture conditions, presumably via negative feedback regulation.[25]

(C) Western blot analyses of CAFs treated with 40 nM PDGFB for 3 days.

(D) Relative growth of CAFs treated with different concentrations of PDGFB for 7 days. The data are presented as mean ± SD ($n = 3$). p values were determined by Student's t test. $^{**}p < 0.01$, $^{***}p < 0.001$.

(E) Western blot analyses of CAFs subjected to Cas9/CRIPSR-mediated knockout with the indicated sgRNAs.

(F) Relative growth of CAFs transduced with the indicated sgRNA and then treated with 20 nM of PDGFB for 7 days. The data are presented as mean ± SD ($n = 3$). p values were determined by Student's t test. Statistically significant differences are indicated. $^{**}p < 0.01$.

(G) Western blot analyses of control and PDGFRB-deficient CAFs that were FACS-sorted on mCherry after incubation with cancer cells for 3 days.

(H) Survival of control and PDGFRB-deficient CAFs that were incubated with cancer cells for 7 days ($n = 3$). $^{**}p < 0.01$, $^{***}p < 0.001$.

(I) Western blot analysis of cancer cells that were FACS-sorted on GFP after incubation for 3 days with control or PDGFRB-deficient CAFs. p values were determined by Student's t test. Statistically significant differences are indicated: $^{**}p < 0.01$, $^{***}p < 0.001$.

(J) Proliferation of cancer cells cultured for 7 days with control or PDGFRB-deficient CAFs in the presence of the indicated concentrations of carboplatin ($n = 3$). $^{***}p < 0.001$.

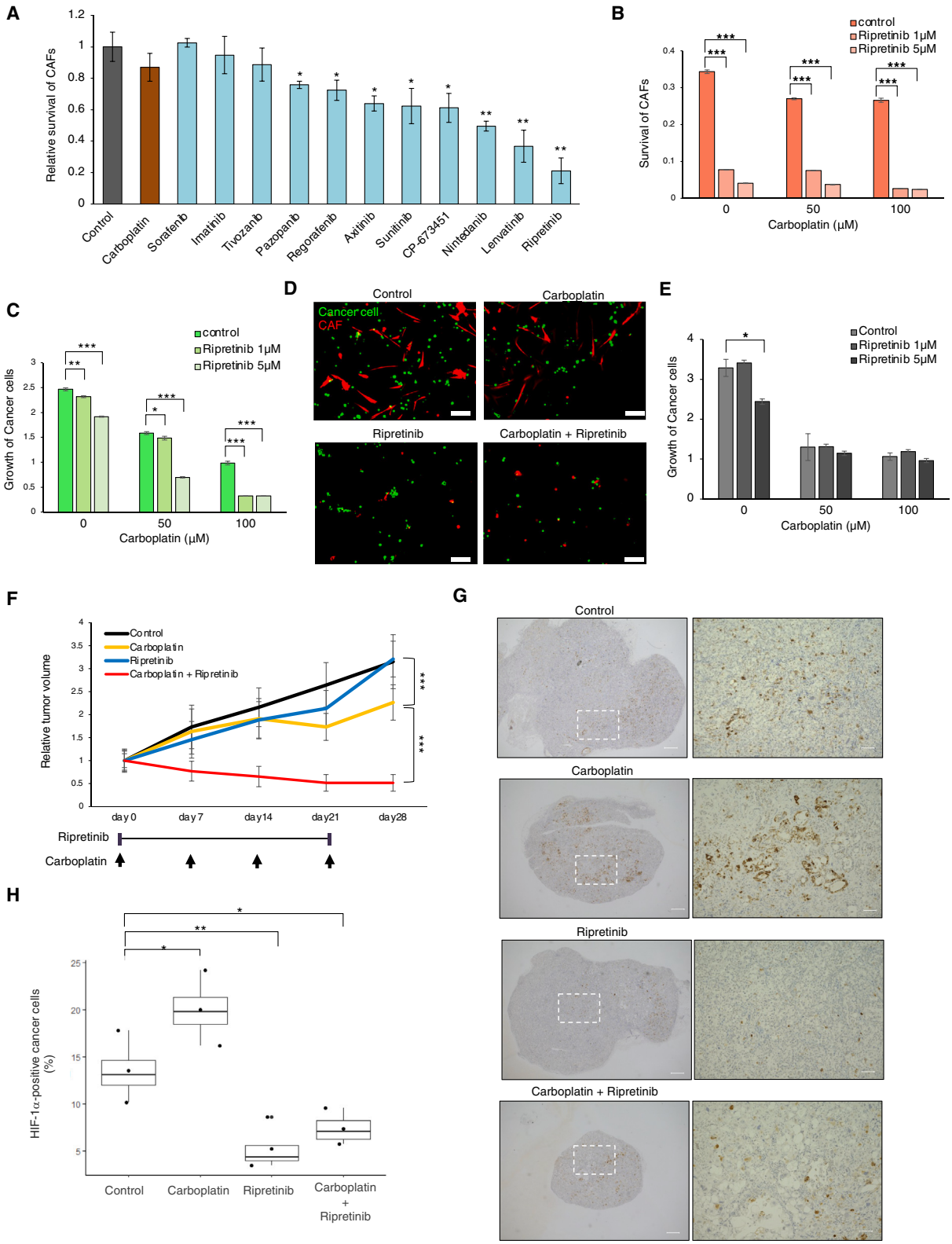

Figure 7. CAF inhibition by ripretinib blocks growth of OCCC in combination with carboplatin

(A) Inhibition of CAFs cultured for 7 days grown on attachment culture conditions in the presence of the indicated TKIs or carboplatin (1 μM). The data are presented as mean ± SD ($n = 3$). p values were determined by Student's t test. Statistically significant differences are indicated: $^{*}p < 0.05$, $^{**}p < 0.01$.

(legend continued on next page)

in vitro. Further investigations at the molecular level revealed that cancer-derived PDGF activates CAFs, which, in turn, induce HIF-1α signaling and chemoresistance in OCCC.

CAFs are involved in cancer progression through interaction with cancer cells and other cell types in the tumor microenvironment.[2,3] Although CAFs are regarded as potential therapeutic targets due to their cancer-promoting roles, effective cancer therapy targeting them is not yet established.[2] This may be due to the heterogeneity of CAFs; there are cancer-promoting and -inhibiting populations, and the biological characteristics of a targetable cancer-promoting CAF subpopulation are not well defined.[2,32]

In this study, we demonstrate that CAF inhibition by ripretinib acts co-operatively with standard chemotherapy to inhibit OCCC tumor growth both in *in vitro* co-culture assays and *in vivo* mouse xenografts. It is noteworthy that, because of frequent oncogenic mutations in *PIK3CA* and other genes affecting phosphatidylinositol 3-kinase-AKT signaling in OCCC, clinical trials have been conducted to examine the efficacy of some TKI inhibitors.[12,33] However, the TKIs used in these trials are intended to directly inhibit proliferation of cancer cells. On the other hand, our data indicate that ripretinib is capable of inhibiting PDGFR activation and survival of CAFs, although the compound may also affect OCCC cells. Considering that the presence of CAFs confers chemoresistance, TKI-mediated inhibition of CAFs may be exploited to overcome OCCC chemoresistance.

It is not clear why ripretinib was better at inhibiting CAFs than other TKIs, but it may be attributed to extensive suppression of PDGFR isoforms and/or related kinases. Indeed, ripretinib blocks PDGFRA (the subunit α isoform), KIT, and BRAF in addition to PDGFRB (the subunit β isoform).[34] The effectiveness of CAF-targeting therapy may also reflect the dominance of cancer-promoting populations within OCCC. In any case, our data suggest that CAF-targeting cancer therapy may be applicable to other types of cancers in which CAFs play a growth-promoting role.

Another salient finding of our study is that CAF activates HIF-1α in a neighboring chemoresistant subpopulation of OCCC. HIF-1α is activated under hypoxic conditions,[35,36] after which its plays an essential role in progression and chemoresistance of a variety of cancers, including EOC.[37,38] By contrast, our data indicate that HIF-1α is induced in OCCC only when cultivated together with CAFs, suggesting that diffusible signals from activated CAFs, not hypoxia itself, induce HIF-1α in OCCC. For example, the induction of HIF-1α may be attributable to cytokines, exosomes, or metabolic products expressed in activated CAFs. Alternatively, it may be attributable to metabolic products. Importantly, HIF-1α is capable of transactivating PDGFB,[39] suggesting that activation of HIF-1α leads to formation of a positive feedback loop between HIF-1α-activated OCCC and CAFs in which PDGFR signaling is activated. HIF-1α induction is associated with chemoresistance from various cancers,[38] and our data suggest that the feedback loop formation between cancer cells and CAFs mediates chemoresistance via HIF-1α induction.

In summary, we show that cancer cell-CAF interactions constitute a chemoresistant niche in the tumor microenvironment of OCCC. Although we focused on CAF functions in this paper, our data do not exclude the possibility that other non-tumor cells, such as macrophages or tumor-infiltrating lymphocytes, also participate in cancer chemoresistance. Comprehensive analyses of the tumor microenvironment, such as neighborhood analyses using multiplexed imaging,[40] will be needed to fully map the complex cell-cell interactions within the tumor microenvironment.

Limitations of the study

To fully establish the functional importance of the interaction between cancer cells and CAFs, a comprehensive co-culture study using a variety of patient-derived cancer spheroids and CAFs is required. In this report, only one CAF and two cancer spheroids were used, mainly due to the difficulty of establishing and expanding patient-derived cells from OCCC. In future, it would be desirable to (1) develop methods to efficiently establish and expand patient-derived cancer spheroids and CAFs from OCCC, (2) firmly establish the functional significance of the cancer cell-CAF interaction, and (3) exploit the established co-culture system to elucidate the molecular basis of the interaction.

STAR★METHODS

Detailed methods are provided in the online version of this paper and include the following:

- KEY RESOURCES TABLE
- RESOURCE AVAILABILITY
  - Lead contact
  - Materials availability
  - Data and code availability
- EXPERIMENTAL MODEL AND STUDY PARTICIPANT DETAILS
  - Clinical samples
  - Establishment of tumor-derived spheroids and CAF
  - Animal experiments
- METHOD DETAILS

(B) Inhibition of CAFs by ripretinib. CAFs co-cultured with cancer cells under co-culture conditions were treated with the indicated concentrations of ripretinib and carboplatin for 7 days ($n = 3$). ***$p < 0.001$.

(C) Co-operative inhibition of the growth of co-cultivated cancer cells (OVN-48) by ripretinib and carboplatin. Cancer cells co-cultured with CAFs were treated for 7 days with the indicated concentrations of ripretinib and carboplatin.

(D) Fluorescence images of cancer cells and CAFs co-cultured for 7 days in the presence or absence of 100 μM carboplatin and/or 5 μM ripretinib. Scale bars, 100 μm.

(E) Cancer cells grown under monoculture conditions were treated with the indicated concentrations of ripretinib and carboplatin for 7 days ($n = 3$). *$p < 0.05$.

(F) Xenografted tumors (OVN-48, 49 days after co-transplantation of cancer cells and CAFs) were treated with the indicated combinations of carboplatin and/or ripretinib, and tumor volume (mean ± standard error of the mean) was measured weekly ($n = 8$). ***$p < 0.001$.

(G) Immunostaining of xenograft tumors (78 days post transplantation) with HIF-1α. Magnified images are shown on the right. Scale bars, 500 μm (right) and 100 μm (left).

(H) Boxplots showing the percentage fraction of HIF-1α-positive cancer cells in the tumor tissues shown in (G). Average values ± SEM are shown. *p* values were determined by Student's t test. Statistically significant differences are indicated: *$p < 0.05$, **$p < 0.01$, ***$p < 0.001$.

SUPPLEMENTAL INFORMATION

Supplemental information can be found online at https://doi.org/10.1016/j.xcrm.2024.101532.

ACKNOWLEDGMENTS

This research was supported by Grant-in-Aids for Scientific Research from the Japan Society for the Promotion of Science (JSPS) under grants JP21H03081 (to K.O.), 18K07283 (to D.S.), and 20K22826 (to Y.M.); the Japan Agency for Medical Research and Development (AMED) under grants JP19cm0106563h0001 and JP21cm0106183h0001 (to K.O.); the Japan Science and Technology Agency (JST) for CREST (Core Research for Evolutional Science and Technology) under grant 21-211035300 (to K.O.); the Japan Health Research Promotion Bureau (JH) under grant 2020-B-03 (to K.O.); JSPS KAKENHI grant 22H04925 (PAGS); and The Vehicle Racing Commemorative Foundation (to K.O.).

AUTHOR CONTRIBUTIONS

K.O. conceived the project. Y.M. oversaw the project. K.O. wrote the initial manuscript, and Y.M. edited the manuscript. Y.M. designed and performed the experiments. H.S. and Y.O. assisted with the *in vivo* experiments. Y.K., D.S., and H.O. assisted with *in vitro* culture. H.U., M.S. and A.H. supported QuPath analyses. H.Y. and Y.Y. performed pathological analyses. T.S., R.T., K. Yamawaki, T.I., T.K., K. Yoshihara, and T.E. provided surgical specimens and clinical information. K.O. and Y.M. provided grant support.

DECLARATION OF INTERESTS

Teikyo University has filed for a patent application on CAF inhibition by tyrosine kinase inhibitors, and K.O. and Y.M. are named as inventors on this patent.

Received: February 22, 2023
Revised: January 4, 2024
Accepted: April 4, 2024
Published: April 25, 2024

REFERENCES

1. Marusyk, A., Janiszewska, M., and Polyak, K. (2020). Intratumor Heterogeneity: The Rosetta Stone of Therapy Resistance. Cancer Cell *37*, 471–484. https://doi.org/10.1016/j.ccell.2020.03.007.
2. Chen, Y., McAndrews, K.M., and Kalluri, R. (2021). Clinical and therapeutic relevance of cancer-associated fibroblasts. Nat. Rev. Clin. Oncol. *18*, 792–804. https://doi.org/10.1038/s41571-021-00546-5.
3. Sahai, E., Astsaturov, I., Cukierman, E., DeNardo, D.G., Egeblad, M., Evans, R.M., Fearon, D., Greten, F.R., Hingorani, S.R., Hunter, T., et al. (2020). A framework for advancing our understanding of cancer-associated fibroblasts. Nat. Rev. Cancer *20*, 174–186. https://doi.org/10.1038/s41568-019-0238-1.
4. Lim, B., Lin, Y., and Navin, N. (2020). Advancing Cancer Research and Medicine with Single-Cell Genomics. Cancer Cell *37*, 456–470. https://doi.org/10.1016/j.ccell.2020.03.008.
5. Rozenblatt-Rosen, O., Regev, A., Oberdoerffer, P., Nawy, T., Hupalowska, A., Rood, J.E., Ashenberg, O., Cerami, E., Coffey, R.J., Demir, E., et al. (2020). The Human Tumor Atlas Network: Charting Tumor Transitions across Space and Time at Single-Cell Resolution. Cell *181*, 236–249. https://doi.org/10.1016/j.cell.2020.03.053.
6. Slyper, M., Porter, C.B.M., Ashenberg, O., Waldman, J., Drokhlyansky, E., Wakiro, I., Smillie, C., Smith-Rosario, G., Wu, J., Dionne, D., et al. (2020). A single-cell and single-nucleus RNA-Seq toolbox for fresh and frozen human tumors. Nat. Med. *26*, 792–802. https://doi.org/10.1038/s41591-020-0844-1.
7. Rao, A., Barkley, D., França, G.S., and Yanai, I. (2021). Exploring tissue architecture using spatial transcriptomics. Nature *596*, 211–220. https://doi.org/10.1038/s41586-021-03634-9.
8. Asp, M., Giacomello, S., Larsson, L., Wu, C., Fürth, D., Qian, X., Wärdell, E., Custodio, J., Reimegård, J., Salmén, F., et al. (2019). A Spatiotemporal Organ-Wide Gene Expression and Cell Atlas of the Developing Human Heart. Cell *179*, 1647–1660.e19. https://doi.org/10.1016/j.cell.2019.11.025.
9. Akhoundova, D., and Rubin, M.A. (2022). Clinical application of advanced multi-omics tumor profiling: Shaping precision oncology of the future. Cancer Cell *40*, 920–938. https://doi.org/10.1016/j.ccell.2022.08.011.
10. Moncada, R., Barkley, D., Wagner, F., Chiodin, M., Devlin, J.C., Baron, M., Hajdu, C.H., Simeone, D.M., and Yanai, I. (2020). Integrating microarray-based spatial transcriptomics and single-cell RNA-seq reveals tissue architecture in pancreatic ductal adenocarcinomas. Nat. Biotechnol. *38*, 333–342. https://doi.org/10.1038/s41587-019-0392-8.
11. Lheureux, S., Gourley, C., Vergote, I., and Oza, A.M. (2019). Epithelial ovarian cancer. Lancet *393*, 1240–1253. https://doi.org/10.1016/S0140-6736(18)32552-2.
12. Shoji, T., Tatsuki, S., Abe, M., Tomabechi, H., Takatori, E., Kaido, Y., Nagasawa, T., Kagabu, M., Baba, T., and Itamochi, H. (2021). Novel Therapeutic Strategies for Refractory Ovarian Cancers: Clear Cell and Mucinous Carcinomas. Cancers *13*, 6120. https://doi.org/10.3390/cancers13236120.
13. De Leo, A., Santini, D., Ceccarelli, C., Santandrea, G., Palicelli, A., Acquaviva, G., Chiarucci, F., Rosini, F., Ravegnini, G., Pession, A., et al. (2021). What Is New on Ovarian Carcinoma: Integrated Morphologic and Molecular Analysis Following the New 2020 World Health Organization Classification of Female Genital Tumors. Diagnostics *11*, 697. https://doi.org/10.3390/diagnostics11040697.
14. Gadducci, A., Multinu, F., Cosio, S., Carinelli, S., Ghioni, M., and Aletti, G.D. (2021). Clear cell carcinoma of the ovary: Epidemiology, pathological and biological features, treatment options and clinical outcomes. Gynecol. Oncol. *162*, 741–750. https://doi.org/10.1016/j.ygyno.2021.06.033.
15. Izar, B., Tirosh, I., Stover, E.H., Wakiro, I., Cuoco, M.S., Alter, I., Rodman, C., Leeson, R., Su, M.J., Shah, P., et al. (2020). A single-cell landscape of high-grade serous ovarian cancer. Nat. Med. *26*, 1271–1279. https://doi.org/10.1038/s41591-020-0926-0.

16. Stur, E., Corvigno, S., Xu, M., Chen, K., Tan, Y., Lee, S., Liu, J., Ricco, E., Kraushaar, D., Castro, P., et al. (2022). Spatially resolved transcriptomics of high-grade serous ovarian carcinoma. iScience *25*, 103923. https://doi.org/10.1016/j.isci.2022.103923.

17. Ma, L., Hernandez, M.O., Zhao, Y., Mehta, M., Tran, B., Kelly, M., Rae, Z., Hernandez, J.M., Davis, J.L., Martin, S.P., et al. (2019). Tumor Cell Biodiversity Drives Microenvironmental Reprogramming in Liver Cancer. Cancer Cell *36*, 418–430.e6. https://doi.org/10.1016/j.ccell.2019.08.007.

18. Stuart, T., Butler, A., Hoffman, P., Hafemeister, C., Papalexi, E., Mauck, W.M., 3rd, Hao, Y., Stoeckius, M., Smibert, P., and Satija, R. (2019). Comprehensive Integration of Single-Cell Data. Cell *177*, 1888–1902.e21. https://doi.org/10.1016/j.cell.2019.05.031.

19. Patel, A.P., Tirosh, I., Trombetta, J.J., Shalek, A.K., Gillespie, S.M., Wakimoto, H., Cahill, D.P., Nahed, B.V., Curry, W.T., Martuza, R.L., et al. (2014). Single-cell RNA-seq highlights intratumoral heterogeneity in primary glioblastoma. Science *344*, 1396–1401. https://doi.org/10.1126/science.1254257.

20. Cummins, E.P., and Taylor, C.T. (2005). Hypoxia-responsive transcription factors. Pflugers Arch. *450*, 363–371. https://doi.org/10.1007/s00424-005-1413-7.

21. Lavie, D., Ben-Shmuel, A., Erez, N., and Scherz-Shouval, R. (2022). Cancer-associated fibroblasts in the single-cell era. Nat. Cancer *3*, 793–807. https://doi.org/10.1038/s43018-022-00411-z.

22. Elyada, E., Bolisetty, M., Laise, P., Flynn, W.F., Courtois, E.T., Burkhart, R.A., Teinor, J.A., Belleau, P., Biffi, G., Lucito, M.S., et al. (2019). Cross-Species Single-Cell Analysis of Pancreatic Ductal Adenocarcinoma Reveals Antigen-Presenting Cancer-Associated Fibroblasts. Cancer Discov. *9*, 1102–1123. https://doi.org/10.1158/2159-8290.CD-19-0094.

23. Vilchez Mercedes, S.A., Bocci, F., Levine, H., Onuchic, J.N., Jolly, M.K., and Wong, P.K. (2021). Decoding leader cells in collective cancer invasion. Nat. Rev. Cancer *21*, 592–604. https://doi.org/10.1038/s41568-021-00376-8.

24. Browaeys, R., Saelens, W., and Saeys, Y. (2020). NicheNet: modeling intercellular communication by linking ligands to target genes. Nat. Methods *17*, 159–162. https://doi.org/10.1038/s41592-019-0667-5.

25. Heldin, C.H., Ostman, A., and Rönnstrand, L. (1998). Signal transduction via platelet-derived growth factor receptors. Biochim. Biophys. Acta *1378*, F79–F113. https://doi.org/10.1016/s0304-419x(98)00015-8.

26. Yerly, L., Pich-Bavastro, C., Di Domizio, J., Wyss, T., Tissot-Renaud, S., Cangkrama, M., Gilliet, M., Werner, S., and Kuonen, F. (2022). Integrated multi-omics reveals cellular and molecular interactions governing the invasive niche of basal cell carcinoma. Nat. Commun. *13*, 4897. https://doi.org/10.1038/s41467-022-32670-w.

27. Satija, R., Farrell, J.A., Gennert, D., Schier, A.F., and Regev, A. (2015). Spatial reconstruction of single-cell gene expression data. Nat. Biotechnol. *33*, 495–502. https://doi.org/10.1038/nbt.3192.

28. Shiokawa, D., Sakai, H., Ohata, H., Miyazaki, T., Kanda, Y., Sekine, S., Narushima, D., Hosokawa, M., Kato, M., Suzuki, Y., et al. (2020). Slow-Cycling Cancer Stem Cells Regulate Progression and Chemoresistance in Colon Cancer. Cancer Res. *80*, 4451–4464. https://doi.org/10.1158/0008-5472.CAN-20-0378.

29. Ohata, H., Shiokawa, D., Obata, Y., Sato, A., Sakai, H., Fukami, M., Hara, W., Taniguchi, H., Ono, M., Nakagama, H., and Okamoto, K. (2019). NOX1-Dependent mTORC1 Activation via S100A9 Oxidation in Cancer Stem-like Cells Leads to Colon Cancer Progression. Cell Rep. *28*, 1282–1295.e8. https://doi.org/10.1016/j.celrep.2019.06.085.

30. Ishiguro, T., Sato, A., Ohata, H., Ikarashi, Y., Takahashi, R.U., Ochiya, T., Yoshida, M., Tsuda, H., Onda, T., Kato, T., et al. (2016). Establishment and Characterization of an In Vitro Model of Ovarian Cancer Stem-like Cells with an Enhanced Proliferative Capacity. Cancer Res. *76*, 150–160. https://doi.org/10.1158/0008-5472.CAN-15-0361.

31. Ohata, H., Ishiguro, T., Aihara, Y., Sato, A., Sakai, H., Sekine, S., Taniguchi, H., Akasu, T., Fujita, S., Nakagama, H., and Okamoto, K. (2012). Induction of the stem-like cell regulator CD44 by Rho kinase inhibition contributes to the maintenance of colon cancer-initiating cells. Cancer Res. *72*, 5101–5110. https://doi.org/10.1158/0008-5472.CAN-11-3812.

32. Biffi, G., and Tuveson, D.A. (2021). Diversity and Biology of Cancer-Associated Fibroblasts. Physiol. Rev. *101*, 147–176. https://doi.org/10.1152/physrev.00048.2019.

33. Katopodis, P., Chudasama, D., Wander, G., Sales, L., Kumar, J., Pandhal, M., Anikin, V., Chatterjee, J., Hall, M., and Karteris, E. (2019). Kinase Inhibitors and Ovarian Cancer. Cancers *11*, 1357. https://doi.org/10.3390/cancers11091357.

34. Dhillon, S. (2020). Ripretinib: First Approval. Drugs *80*, 1133–1138. https://doi.org/10.1007/s40265-020-01348-2.

35. Semenza, G.L. (2012). Hypoxia-inducible factors in physiology and medicine. Cell *148*, 399–408. https://doi.org/10.1016/j.cell.2012.01.021.

36. Kaelin, W.G., Jr., and Ratcliffe, P.J. (2008). Oxygen sensing by metazoans: the central role of the HIF hydroxylase pathway. Mol. Cell *30*, 393–402. https://doi.org/10.1016/j.molcel.2008.04.009.

37. Wang, X., Du, Z.W., Xu, T.M., Wang, X.J., Li, W., Gao, J.L., Li, J., and Zhu, H. (2021). HIF-1alpha Is a Rational Target for Future Ovarian Cancer Therapies. Front. Oncol. *11*, 785111. https://doi.org/10.3389/fonc.2021.785111.

38. Doktorova, H., Hrabeta, J., Khalil, M.A., and Eckschlager, T. (2015). Hypoxia-induced chemoresistance in cancer cells: The role of not only HIF-1. Biomed. Pap. Med. Fac. Univ. Palacky Olomouc Czech. Repub. *159*, 166–177. https://doi.org/10.5507/bp.2015.025.

39. Schito, L., Rey, S., Tafani, M., Zhang, H., Wong, C.C.L., Russo, A., Russo, M.A., and Semenza, G.L. (2012). Hypoxia-inducible factor 1-dependent expression of platelet-derived growth factor B promotes lymphatic metastasis of hypoxic breast cancer cells. Proc. Natl. Acad. Sci. USA *109*, E2707–E2716. https://doi.org/10.1073/pnas.1214019109.

40. Schürch, C.M., Bhate, S.S., Barlow, G.L., Phillips, D.J., Noti, L., Zlobec, I., Chu, P., Black, S., Demeter, J., McIlwain, D.R., et al. (2020). Coordinated Cellular Neighborhoods Orchestrate Antitumoral Immunity at the Colorectal Cancer Invasive Front. Cell *182*, 1341–1359.e19. https://doi.org/10.1016/j.cell.2020.07.005.

41. Kato, M., Nakamura, H., Nagai, M., Kubo, T., Elzawahry, A., Totoki, Y., Tanabe, Y., Furukawa, E., Miyamoto, J., Sakamoto, H., et al. (2018). A computational tool to detect DNA alterations tailored to formalin-fixed paraffin-embedded samples in cancer clinical sequencing. Genome Med. *10*, 44. https://doi.org/10.1186/s13073-018-0547-0.

42. Butler, A., Hoffman, P., Smibert, P., Papalexi, E., and Satija, R. (2018). Integrating single-cell transcriptomic data across different conditions, technologies, and species. Nat Biotechnol *36*, 411–420. https://doi.org/10.1038/nbt.4096.

43. Yu, G., Wang, L.G., Han, Y., and He, Q.Y. (2012). clusterProfiler: an R package for comparing biological themes among gene clusters. OMICS *16*, 284–287. https://doi.org/10.1089/omi.2011.0118.

44. Alvarez, M.J., Shen, Y., Giorgi, F.M., Lachmann, A., Ding, B.B., Ye, B.H., and Califano, A. (2016). Functional characterization of somatic mutations in cancer using network-based inference of protein activity. Nat Genet *48*, 838–847. https://doi.org/10.1038/ng.3593.

45. Garcia-Alonso, L., Holland, C.H., Ibrahim, M.M., Turei, D., and Saez-Rodriguez, J. (2019). Benchmark and integration of resources for the estimation of human transcription factor activities. Genome Res. *29*, 1363–1375. https://doi.org/10.1101/gr.240663.118.

46. Therneau, T.M., and Grambsch, P.M. (2000). Estimating the Survival and Hazard Functions. In Modeling Survival Data:Extending the Cox Model (New York: Springer), pp. 7–37. https://doi.org/10.1007/978-1-4757-3294-8_2.

47. Browaeys, R., Saelens, W., and Saeys, Y. (2020). NicheNet: modeling intercellular communication by linking ligands to target genes. Nat Methods *17*, 159–162. https://doi.org/10.1038/s41592-019-0667-5.

48. Bankhead, P., Loughrey, M.B., Fernández, J.A., Dombrowski, Y., McArt, D.G., Dunne, P.D., McQuaid, S., Gray, R.T., Murray, L.J., Coleman, H.G., et al. (2017). QuPath: Open source software for digital pathology image analysis. Sci. Rep. *7*, 16878. https://doi.org/10.1038/s41598-017-17204-5.

49. Schmidt, U., Weigert, M., Broaddus, C., Myers, G., (2018). Cell Detection with Star-Convex Polygons. In Lecture Notes in Computer Science, (Springer International Publishing), pp. 265–273. https://doi.org/10.1007/978-3-030-00934-2_30.

50. Stoltzfus, C.R., Filipek, J., Gern, B.H., Olin, B.E., Leal, J.M., Wu, Y., Lyons-Cohen, M.R., Huang, J.Y., Paz-Stoltzfus, C.L., Plumlee, C.R., et al. (2020). CytoMAP: A Spatial Analysis Toolbox Reveals Features of Myeloid Cell Organization in Lymphoid Tissues. Cell Rep. *31*, 107523. https://doi.org/10.1016/j.celrep.2020.107523.

51. Tamura, R., Yoshihara, K., Matsuo, K., Yachida, N., Miyoshi, A., Takahashi, K., Sugino, K., Yamaguchi, M., Mori, Y., Suda, K., et al. (2021). Proposing a molecular classification associated with hypercoagulation in ovarian clear cell carcinoma. Gynecol. Oncol. *163*, 327–333. https://doi.org/10.1016/j.ygyno.2021.08.009.

52. Hu, Z., Artibani, M., Alsaadi, A., Wietek, N., Morotti, M., Shi, T., Zhong, Z., Santana Gonzalez, L., El-Sahhar, S., Carrami, E.M., et al. (2020). The Repertoire of Serous Ovarian Cancer Non-genetic Heterogeneity Revealed by Single-Cell Sequencing of Normal Fallopian Tube Epithelial Cells. Cancer Cell *37*, 226–242.e7. https://doi.org/10.1016/j.ccell.2020.01.003.

53. Luo, H., Xia, X., Huang, L.B., An, H., Cao, M., Kim, G.D., Chen, H.N., Zhang, W.H., Shu, Y., Kong, X., et al. (2022). Pan-cancer single-cell analysis reveals the heterogeneity and plasticity of cancer-associated fibroblasts in the tumor microenvironment. Nat. Commun. *13*, 6619. https://doi.org/10.1038/s41467-022-34395-2.

54. Subramanian, A., Tamayo, P., Mootha, V.K., Mukherjee, S., Ebert, B.L., Gillette, M.A., Paulovich, A., Pomeroy, S.L., Golub, T.R., Lander, E.S., and Mesirov, J.P. (2005). Gene set enrichment analysis: a knowledge-based approach for interpreting genome-wide expression profiles. Proc. Natl. Acad. Sci. USA *102*, 15545–15550. https://doi.org/10.1073/pnas.0506580102.

55. Yu, G., Wang, L.G., Han, Y., and He, Q.Y. (2012). clusterProfiler: an R package for comparing biological themes among gene clusters. OMICS *16*, 284–287. https://doi.org/10.1089/omi.2011.0118.

56. Hafemeister, C., and Satija, R. (2019). Normalization and variance stabilization of single-cell RNA-seq data using regularized negative binomial regression. Genome Biol. *20*, 296. https://doi.org/10.1186/s13059-019-1874-1.

57. Stevens, M., Nanou, A., Terstappen, L.W.M.M., Driemel, C., Stoecklein, N.H., and Coumans, F.A.W. (2022). StarDist Image Segmentation Improves Circulating Tumor Cell Detection. Cancers *14*, 2916. https://doi.org/10.3390/cancers14122916.

58. Uwe Schmidt, M.W., Coleman, B., and Myers, G. (2018). Cell Detection with Star-convex Polygons. In International Conference on Medical Image Computing and Computer-Assisted Intervention (MICCAI). https://doi.org/10.48550/arXiv.1806.03535.

STAR★METHODS

KEY RESOURCES TABLE

REAGENT or RESOURCE	SOURCE	IDENTIFIER
Antibodies		
Rabbit anti-human PAX8	Proteintech	Cat# 10336-1-AP, RRID: AB_2236705
Mouse anti-human Cytokeratin 7	Dako	Cat# M7018, RRID: AB_2134589
Mouse anti-human α-SMA	Abcam	Cat# ab7817, RRID: AB_262054
Rabbit anti-human Collagen I	Abcam	Cat# ab138492, RRID: AB_2861258
Mouse anti-human β-Actin	Sigma-Aldrich	Cat# A5316, RRID: AB_476743
Rabbit anti-human HIF-1α	Abcam	Cat# ab51608, RRID: AB_880418
Rabbit anti-human HIF-2α	Abcam	Cat# ab199, RRID: AB_302739
Rabbit anti-human PDGFB	Abcam	Cat# ab23914, RRID: AB_2162180
Rabbit anti-human Fibronectin	Abcam	Cat# ab268020, RRID: AB_2941028
Rabbit anti-human PDGFRβ	Cell Signaling Technology	Cat# 3169, RRID: AB_2162497
Rabbit anti-human PDGFRβ (phospho Y1021)	Abcam	Cat# ab16868, RRID: AB_302554
Rabbit anti-human FAP-α	Abcam	Cat# ab53066, RRID: AB_880077
Goat Anti-Rabbit IgG Antibody (H + L), Biotinylated	Vector Laboratories	Cat# BA-1000, RRID: AB_2313606
Donkey anti-rabbit IgG Alexa Fluor 750	Abcam	Cat# ab175728, RRID: AB_2924801
Goat anti-mouse IgG Alexa Fluor 555	Thermo Fisher Scientific	Cat# A-21424, RRID: AB_141780
Rabbit anti-human FAP-α	Abcam	Cat# ab227703
Biological samples		
Ovarian clear cell carcinoma tissue samples	National Cancer Center Japan, Niigata University	N/A
Mouse xenograft tumors	National Cancer Center Japan	N/A
Chemicals, peptides, and recombinant proteins		
ProLongTM Diamond Antifade Mountant with DAPI	Thermo Fisher Scientific	Cat# P36971
3,3′-diaminobenzidine	Sigma-Aldrich	Cat# D12384
Nuclei EZ Lysis buffer	Sigma-Aldrich	Cat# NUC-101
Recombinant RNase Inhibitor	Clontech/TaKaRa	Cat# 2313A
Collagenase/hyaluronidase	Stemcell Technologies	Cat# 7912
Histodenz	Sigma-Aldrich	Cat# D2158
ACK Lysing Buffer	Thermo Fisher Scientific	Cat# A1049201
STEMPRO hESC SFM	Thermo Fisher Scientific	Cat# A1000701
basic fibroblast growth factor	Thermo Fisher Scientific	Cat# AA10-155
Accumax	Innovative Cell Technologies	Cat# AM105
MEM-α	Thermo Fisher Scientific	Cat# 12561-5
Fetal Bovine Serum	Thermo Fisher Scientific	Cat# 10270106
TripLE Express Enzyme	Thermo Fisher Scientific	Cat# 12604013
DMEM/F12-GlutaMAX	Thermo Fisher Scientific	Cat# 10565-042,
HEPES	Thermo Fisher Scientific	Cat# 15630106
N-2 Supplement	Thermo Fisher Scientific	Cat# 17502-001
B-27 supplement	Thermo Fisher Scientific	Cat# 17504-001
Human EGF	Thermo Fisher Scientific	Cat# PHG0313
N-acetylcysteine	Sigma-Aldrich	Cat# A7250
Growth Factor Reduced Matrigel	Corning	Cat# 356231

(*Continued on next page*)

Continued

REAGENT or RESOURCE	SOURCE	IDENTIFIER
Cell Recovery Solution	Corning	Cat# 354253
Human Recombinant PDGFB	Fuji Film Wako	Cat# 160-24033
Carboplatin	Selleck Chemicals	Cat# S1215
CP-673451	Selleck Chemicals	Cat# S1536
Sorafenib	Selleck Chemicals	Cat# S7397
Imatinib	Selleck Chemicals	Cat# S2475
Regorafenib	Selleck Chemicals	Cat# S1178
Tivozanib	Selleck Chemicals	Cat# S1207
Pazopanib	Selleck Chemicals	Cat# S3012
Axitinib	Selleck Chemicals	Cat# S1005
Sunitinib	Selleck Chemicals	Cat# S7781
Nintedanib	Selleck Chemicals	Cat# S1010
Lenvatinib	Selleck Chemicals	Cat# S1164
Ripretinib	Selleck Chemicals	Cat# S8757
Alexa Fluor™ 488 Tyramide Reagent	Thermo Fisher Scientific	Cat# B40953
ProLong Glass Antifade Mountant	Thermo Fisher Scientific	Cat# P36984
Critical commercial assays		
Vectastain Elite ABC detection kit	Vector Laboratories	Cat# PK-6100
Chromium Single Cell 3′ Reagent Kit v3	10x Genomics	Cat# PN-1000075
Visium Spatial Tissue Optimization Kit	10x Genomics	Cat# PN-1000193
3′ CellPlex Kit Set A	10x Genomics	Cat# PN-1000261
DNeasy Blood & Tissue kit	Qiagen	Cat# 69504
SureSelectXT reagent kit	Agilent	Cat# G9611A
SureSelect NCC Oncopanel	Agilent	Cat# 931195
Dual Luciferase Reporter Assay System	Promega	Cat# E1960
CellTiter-Glo Luminescent Cell Viability Assays	Promega	Cat# G7571
Opal 6-Plex Detection kit	Akoya Biosciences	Cat# NEL871001KT
Deposited data		
Ovarian clear cell carcinoma *in vitro* scRNA-seq data	Gene Expression Omnibus	GSE224333
Ovarian clear cell carcinoma snRNA-seq data	Gene Expression Omnibus	GSE224334
Ovarian clear cell carcinoma visium data	Gene Expression Omnibus	GSE224335
Experimental models: Organisms/strains		
NOD/Shi-scid IL-2Rγnull mice	Japan Crea	N/A
Oligonucleotides		
Edit-R Synthetic sgRNA Non-targeting Control #1	Dharmacon-Horizon Discovery	Cat# U-009501-01-001p
Edit-R Human Synthetic sgRNA pool for PDGFRB	Dharmacon-Horizon Discovery	Cat# SQ-003163-01-0002
Recombinant DNA		
pCDH-CMV-MCS-EF1α-copGFP	System biosciences	Cat# CD511B-1
pGL4.51[luc2/CMV/*Neo*]	Promega	Cat# E1320
pcDNA5-MTS-TagBFP-P2AT2A-EGFP-NLS-P2AT2A-mCherry-PTS1	Addgene	Cat# 87829
pGL4.74[*hRluc*/TK]	Promega	Cat# E6921
Software and algorithms		
CellRanger version 3.0.2	10x Genomics	https://www.10xgenomics.com
SpaceRanger version 1.1.0	10x Genomics	https://www.10xgenomics.com
cisCall	Kato et al.[41]	https://www.ciscall.org/
CellRanger version 6.1.2	10x Genomics	https://www.10xgenomics.com
Seurat version 3.2.2	Butler et al.[42]; Stuart et al.[18]	https://github.com/satijalab/seurat

(*Continued on next page*)

Continued

REAGENT or RESOURCE	SOURCE	IDENTIFIER
InferCNV version 1.5.0	N/A	https://github.com/broadinstitute/inferCNV
escape version 1.8.0	N/A	https://github.com/ncborcherding/escape
clusterProfiler	Yu et al.[43]	https://github.com/YuLab-SMU/clusterProfiler
VIPER version 1.30.0	Alvarez et al.[44]	https://www.bioconductor.org/packages/release/bioc/html/viper.html
DoRothEA version 1.6.0	Garcia-Alonso et al.[45]	https://github.com/saezlab/DoRothEA
survival	Therneau and Grambsch[46]	https://cran.r-project.org/web/packages/survival/index.html
igraph	N/A	https://CRAN.R-project.org/package=igraph
NicheNet	Browaeys et al.[47]	https://github.com/saeyslab/nichenetr
QuPath	Bankhead et al.[48]	https://qupath.github.io/
StarDist	Schmidt et al.[49]	https://github.com/stardist/stardist
CytoMAP	Stoltzfus et al.[50]	https://gitlab.com/gernerlab/cytomap

RESOURCE AVAILABILITY

Lead contact

Further information and requests for resources and reagents should be directed to and will be fulfilled by the lead contact, Koji Okamoto (okamoto.kouji.dm@teikyo-u.ac.jp).

Materials availability

Plasmid vectors generated in this study are available from the lead contact upon request with a materials transfer agreement.

Data and code availability

Accession numbers of RNA-seq data (GSE224333, GSE224334, GSE224335) are listed in the key resources table. This paper does not report original code. Any additional information required to reanalyze the data reported in this paper is available from the lead contact upon request.

EXPERIMENTAL MODEL AND STUDY PARTICIPANT DETAILS

Clinical samples

All procedures were performed using protocols reviewed and approved by the Ethics Committee of Teikyo University, Niigata University, and the National Cancer Center. All participants provided informed consent. For the snRNA-seq and spatial transcriptomics, surgical specimens were obtained from patients between the ages of 44–72 (median age: 56), and their baseline characteristics was provided in Table S1. For the Vectra multi-color analyses, surgical specimens were obtained from patients between the ages of 25–78 (median age: 55). Isolated surgical specimens were stored in at −80°C, subjected to formalin-fixed paraffin-embedded (FFPE) analyses, or used for establishment of cancer spheroids or CAFs.

Establishment of tumor-derived spheroids and CAF

To establish patient-derived cancer spheroids (OVN-48 and OVN-43), OCCC tissues obtained by surgical excision were washed immediately with PBS, cut into ∼10 mm^3 pieces using a scalpel, and dissociated with collagenase/hyaluronidase (#7912, Stem Cell Technologies) for 2 h at 37°C. Dissociated cells were filtered sequentially through 100- and 70-μm cell strainers (352350, BD Falcon) and isolated by density gradient centrifugal purification in PBS containing Histodenz (D2158, Sigma).[29] After lysis of red blood cells with ACK Lysing Buffer (A1049201, Thermo Fisher Scientific), the isolated cells were used to establish cancer spheroids by cultivating them on ultra-low-attachment culture dishes (#3471 or #3262, Corning) in STEMPRO hESC SFM (A1000701, Thermo Fisher Scientific) supplemented with 8 ng/mL basic fibroblast growth factor (#AA10-155, Thermo Fisher Scientific) and penicillin/streptomycin (37°C, 5% CO_2). Serial passage of formed cancer spheroids was performed every 2 weeks by dissociating the spheroids with Accumax (AM105, Innovative Cell Technologies). To establish CAF cultures, the red blood cell-removed Histodenz-purified cells were grown on attachment culture dishes (#35003, Corning) in MEM-α (#12561-05, Thermo Fisher Scientific) containing 10% FBS (#10270106, Thermo Fisher Scientific) and penicillin/streptomycin (37°C, 5% CO_2). For serial passage of established CAFs, attached cells were dissociated with TripLE Express Enzyme (#12604013, Thermo Fisher Scientific) every 2 weeks.

Animal experiments

All procedures of mouse experiments were performed using protocols reviewed and approved by the Institutional Animal Care and Use Committee of Teikyo University and the National Cancer Center. To examine the synergistic effects of Carboplatin and Ripretinib on xenograft tumors, Luc2-GFP-labeled cancer spheroid cells and HRluc-mCherry-labeled CAFs were dissociated and mixed at a 1:1 ratio. Next, 1×10^5 mixed cells were suspended in 100 μL of E medium containing 50% GFR Matrigel, and injected subcutaneously into the flanks of NOG (NOD/Shi-scid IL-2Rγnull) mice (Japan Crea). At 49 days post-transplantation (tumor volume: ~100 mm^3), mice were randomized into four groups and with/without Carboplatin (40 mg/kg per week, intraperitoneal injection) and/or Ripretinib (50 mg/kg/day, oral administration) for an additional 28 days. Tumor volume was calculated weekly using the standard formula: length × width × height × π/6). Evaluation of tumor volume according to luciferase activity was performed using the IVIS Spectrum imaging system (Caliper Life Science), which measured total luminescence emitted from the area of the mouse abdomen (photons/sec/cm2/sr) at 10 min post-intraperitoneal administration of 15 mg/mL D-luciferin potassium salt (10 μL per 1 g body weight, Wako). The data were analyzed using Living Image software (v. 4.2; Caliper Life Science).

METHOD DETAILS

Nucleus isolation

Frozen OCCC samples were homogenized in 500 μL of ice-cold Nuclei EZ Lysis buffer (NUC-101, Sigma-Aldrich) using a KIMBLE Dounce tissue grinder (D8938, Sigma-Aldrich), and incubated on ice for 5 min with an additional 1 mL of the lysis buffer. The homogenate was filtered through a 70-μm cell strainer (#352350, Corning) and then centrifuged at 500×*g* for 1 min at 4°C. The pellet was resuspended, washed with 1 mL of Lysis buffer, and incubated on ice for 5 min. After another cycle of washing with Lysis buffer, the pellet was washed twice in 1 mL of Nuclei Suspension Buffer (1× PBS, 1% BSA, and 0.2% RNase inhibitor (2313A, Clontech/TaKaRa)). The nuclear pellet was resuspended in 1 mL of Nuclei Suspension Buffer and filtered twice through a 35-μm cell strainer (#352235, Corning).

Single-nucleus RNA-seq (snRNA-seq)

For snRNA-seq of OCCC tissues, cDNA libraries were prepared from isolated nuclei (4000–8000 nuclei) on Chromium controller (10X Genomics) using the Single Cell 3′ Reagent Kit v3 (PN-1000075, 10X Genomics). Next-generation sequencing of the cDNA libraries was performed on the HiSeq 2500 (Illumina) platform at a median depth of 65,124 reads/cell. Fastq files of the sequencing data were processed by the cellranger pipeline (version 3.0.2, 10X Genomics) and mapped to the GRCh38 (version 3.0.0 for premRNA) reference genome to generate matrices of unique molecular identifier (UMI) and cell-associated barcodes.

Spatial transcriptomics

Frozen OCCC samples were embedded in pre-chilled OCT compound (#25608-930, Sakura Finetek Japan Co., Ltd.), re-frozen on dry ice, and then stored at −80°C. Preparation of cDNA libraries from the tissue sections was performed using a Visium Spatial Gene Expression kit (10X Genomics) according to the manufacturer's instructions. Optimal parameters for permeabilization of OCCC tissue were determined using the Visium Spatial Tissue Optimization Kit (PN-1000193; 10x Genomics). Subsequently, 10 μm sections cut from OCT-embedded samples were subjected to H&E staining and cDNA library preparation from barcoded Visium spots after permeabilization for 20 min. Next-generation sequencing was performed on a HiSeq 2500 (Illumina) platform. Fastq files of the sequencing data were processed by the spaceranger pipeline (version 1.1.0., 10X Genomics) and mapped to the GRCh38 reference genome to generate matrices of UMI and spot-associated barcodes.

Targeted genome sequencing

Genomic DNA was extracted from frozen OCCC tissues using a DNeasy Blood & Tissue kit (#69504, Qiagen) prior to selection of targeted sequences using the SureSelect NCC Oncopanel (v.4.0; Agilent Technologies). The captured sequences were subsequently used to construct libraries using a SureSelectXT reagent kit (Agilent Technologies). Paired-end sequencing (2 × 150 bp) was performed by using NextSeq 500 (Illumina). Mutations (single-nucleotide variations, and short insertions, and deletions), gene amplifications, and gene fusions, were detected using the cisCall system.[41]

Bulk RNA-seq analysis

Total RNA extraction and library preparation were performed as previously reported.[51] Briefly, total RNA was extracted from frozen samples of OCCC (30 cases) using TRIzol (#15596026, Invitrogen), and then subjected to cDNA library preparation by using a TruSeq Stranded mRNA Library Prep Kit (RS-20020595, Illumina), according to the manufacturer's instructions. Subsequently, cDNA libraries were sequenced on the Illumina HiSeq 2500 platform with the 2 × 100-bp paired-end read module. Sequenced reads were mapped onto the human genome reference sequence (UCSU hg19) using Basespace (Illumina).

Plasmid construction

To generate the pCDH-Luc2-T2A-copGFP plasmid, the Luc2-T2A-copGFP cassette was initially generated by ligating a synthesized T2A sequence to Luc2 (PCR-amplified from pGL4.51[Luc2/CMV/*Neo*] (Promega, E1320)) and copGFP (PCR-amplified from

pCDH-CMV-MCS-EF1α-copGFP (System biosciences, CD511B-1)). Subsequently, the Luc2-T2A-TagBFP sequence in pCDH-Luc2-T2A-TagBFP[28] was substituted with the Luc2-T2A-copGFP cassette via the *EcoRI* and *SalI* sites to generate pCDH-Luc2-T2A-copGFP. To generate the pCDH-hRluc-T2A-mCherry plasmid, the hRluc-T2A-mCherry cassette was first generated by ligating the synthesized T2A sequence with hRluc (PCR-amplified from pGL4.74[hRluc/TK] (Promega, E6921)) and mCherry (PCR-amplified from pcDNA5-MTS-TagBFP-P2AT2A-EGFP-NLS-P2AT2A-mCherry-PTS1 (Addgene, #87829)). Subsequently, pCDH-hRluc-T2A-mCherry was generated from pCDH-Luc2-T2A-TagBFP using a similar construction strategy. The pCDH-Luc2-T2A-copGFP and pCDH-hRluc-T2A-mCherry plasmids were used to generate lentiviruses for gene transduction into cancer cells and CAF, respectively.

In vitro co-culture assay

OCCC spheroid cells and CAF were infected by lentiviruses expressing Luc2 and GFP (pCDH-Luc2-T2A-copGFP), and lentiviruses expressing hRLuc and mCherry (pCDH-hRLuc-T2A-mCherry), respectively. For co-culture, the infected spheroid cells and CAF were mixed at 1:1 ratio. Subsequently, monocultured cancer cells, monocultured CAF, or co-cultured cells were plated into a 96-well plate (1×10^4 cells/well) layered with growth factor-reduced (GFR) Matrigel (#356231, Corning), and then incubated for 6 h with MEM-α supplemented with 10% FBS. After removing floating dead cells, the remaining cells were overlaid with GFR Matrigel and, subsequently, with E medium (DMEM/F12-GlutaMAX (#10565-042, Thermo Fisher Scientific)) supplemented with penicillin-streptomycin, 10 mM HEPES (#15630106, Thermo Fisher Scientific), *N*-2 Supplement (#17502-001, Thermo Fisher Scientific), B-27 supplement (#17504-001, Thermo Fisher Scientific), 1 mM N-acetylcysteine (A7250, Sigma-Aldrich), and 50 ng/mL human EGF (PHG0313, Thermo Fisher Scientific)). For the chemosensitivity assay, monocultured or co-cultured cells were treated with Carboplatin (S1215, Selleck Chemicals). Cell growth was evaluated using a dual luciferase reporter kit (E1960, Promega). For western blot analysis, cultivated cells were harvested with Cell Recovery Solution (#354253, Corning) and GFP-expressing cancer cells and mCherry-expressing CAFs were selected by flow cytometry (FACS Aria III, Beckton Dickinson, Franklin Lakes, New Jersey).

Single-cell RNA-seq (scRNA-seq) of *in vitro*-cultivated cells

Monoculture and co-culture of cancer cells and CAF (3 days after incubation) were used to prepare single-cell cDNA libraries. For this, 3000–6000 cells were applied to a Chromium controller (10X Genomics). Library construction was performed using the Single Cell 3′ Reagent Kit v3 and 3′ CellPlex Kit Set A (10X Genomics), according to the manufacturer's instructions. Next-generation sequencing of the cDNA libraries was performed using a HiSeq 2500 (Illumina). Fastq files of the sequencing data were processed by the cellranger pipeline (version 6.1.2, 10X Genomics) using the command "cellranger multi", and then mapped onto the GRCh38 reference genome to generate matrices of UMI and cell-associated barcodes.

In vitro proliferation assays of CAF

To examine the chemosensitivity of CAF, *in vitro*-cultivated CAFs at Day 7–10 post-passage were enzymatically dissociated and used for chemosensitivity assays. The following TKIs were purchased from Selleck Chemicals and used for the assay: CP-673451 (S1536), Sorafenib (S7397), Imatinib (S2475), Regorafenib (S1178), Tivozanib (S1207), Pazopanib (S3012), Axitinib (S1005), Sunitinib (S7781), Nintedanib (S1010), Lenvatinib (S1164), and Ripretinib (S8757). Human recombinant PDGFB (160–24033, Fuji Film Wako) was used to examine the effects of PDGF signaling on CAF. The effects of TKIs or PDGFB on cell growth were quantified by measuring luciferase activity in a CellTiter-Glo Luminescent Cell Viability Assay (G7571, Promega) according to the manufacturer's instructions.

CRISPR/Cas9-mediated gene knockout

CAFs grown for 7–10 days after passaging were enzymatically dissociated and subjected to Cas9-mediated gene knockout using the Neon Transfection System (Thermo Fisher Scientific), according to the manufacturer's instructions. The sgRNA/Cas9 complex formed after mixing Cas9 protein (Invitrogen) with Edit-R Human Synthetic sgRNA pool for PDGFRB (SQ-003163-01-0002, Dharmacon-Horizon Discovery) or Edit-R Synthetic sgRNA Non-targeting Control #1 (U-009501-01-001p, Dharmacon-Horizon Discovery) was used for electroporation (1600 V, 10 ms, two pulses).

Western blot analyses

Western blot analyses were performed as previously described.[30] Antibodies specific for the following markers were purchased from the indicated suppliers: PAX8 (10336-1-AP, Proteintech; dilution, 1:2000), Cytokeratin 7 (M7018, Dako; 1:1000), α-SMA (ab7817, abcam; 1:3000), Collagen I (ab138492, abcam; 1:1000), β-Actin (A5316, Sigma-Aldrich; 1:1000), HIF-1α (ab51608, abcam; 1:1000), HIF-2α (ab199, abcam; 1:1000), PDGFB (ab23914, abcam; 1:1000), Fibronectin (ab268020, abcam; 1:1000), PDGFRB (#3169, Cell Signaling Technology; 1:1000), PDGFRB (phospho Y1021; ab16868, abcam; 1:1000), FAP-α (ab53066, abcam; 1:1000).

Immunofluorescence analysis of clinical specimens

To immunostain clinical samples of OCCC, surgical specimens were fixed in 10% formaldehyde, embedded in paraffin, and sliced into 4-μm sections. For histological examination, sections were stained with H&E. For immunofluorescence analyses, sections were subjected to antigen retrieval with 10 mM citric acid buffer (pH 6.0), followed by blocking of endogenous peroxidase activity with 0.3% hydrogen peroxide. For co-staining with PAX8, HIF-1α, and α-SMA, slides were stained sequentially with a rabbit anti-PAX8

antibody (1:1000; Proteintech, 10336-1-AP), biotinylated-goat anti-rabbit IgG (1:500; Vector Laboratories, BA-1000), the Vectastain Elite ABC detection kit (Vector Laboratories, PK-6100), and Alexa Fluor 488 Tyramide Reagent (Invitrogen, B40953). For consecutive staining with anti-HIF-1α and anti-α-SMA antibodies, slides were boiled in 10 mM citric acid buffer (pH 6.0) for >15 min to remove the PAX8-secondary antibody complex. Slides were then stained with a rabbit anti-HIF-1α antibody (1:100; abcam, ab51608) and a mouse anti-α-SMA antibody (1:600; abcam, ab7817), followed by donkey anti-rabbit IgG AlexaFluor 750-conjugated (1:1000; abcam, ab175728) or goat anti-mouse IgG- AlexaFluor 555-conjugated (1:1000; Invitrogen, A21424) secondary antibodies. The immunostained slides were then mounted using ProLong Diamond Antifade Mountant containing DAPI (Invitrogen, P36971). The same procedure was used for immunostaining with anti-KRT7, anti-α-SMA, and anti-PDGFRB (phospho Y1021) antibodies (Figure S7B). Antibodies specific for the following markers were purchased from the listed suppliers: cytokeratin 7 (M7018, Dako, 1:100), α-SMA (ab7817, abcam, 1:600), and PDGFRB (phospho Y1021) (ab16868, abcam, 1:100). Immunofluorescence images were evaluated by Vectra Polaris (Akoya Biosciences).

Immunofluorescence analysis of *in vitro*-cultivated cells

Cancer cells under monoculture conditions or under co-culture conditions with CAF were plated on GFR Matrigel-coated glass-bottom dishes (D11140H, Matsunami Glass Ind.), fixed with cold methanol, and permeabilized with 0.1% Triton X-(Sigma-Aldrich). After blocking with 5% BSA, fixed cells were incubated with rabbit anti-HIF-1α (1:100; abcam, ab51608) and mouse anti-α-SMA (1:600; abcam, ab7817) antibodies, followed by donkey anti-rabbit IgG AlexaFluor 750-conjugated (1:1000; abcam, ab175728) or goat anti-mouse IgG AlexaFluor 555-conjugated (1:1000; Invitrogen, A21424). Subsequently, cells were mounted in ProLong Diamond Antifade Mountant with DAPI (Invitrogen, P36971). Fluorescence images were taken under a Keyence BZ-800 Microscope (Keyence).

Immunohistochemical staining

Clinical tumor samples and mouse xenograft tumors were fixed in neutral formalin and embedded in paraffin. Immunohistochemical staining was performed as previously described.[30] Briefly, sections were used for H&E staining or immunostaining with primary anti-FAP-α (ab53066, abcam, 1:100), anti-HIF-1α (ab51608, abcam, 1:100) or anti-α-SMA (ab7817, abcam, 1:500) antibodies, followed by staining with biotinylated secondary antibodies (Vector Laboratories) and incubation with The Vector stain ABC kit (PK6100, Vector Laboratories) and 3,3′-diaminobenzidine (D12384, Sigma). For evaluation of HIF-1α staining, positive cells in four representative areas were counted using Hybrid Cell Count software (Keyence).

Multi-color immunostaining by Vectra Polaris

For multi-colored immunofluorescence, formalin fixed paraffin-embedded sections (4-μm) were stained on a BondRX automated stainer (Leica) with Opal 6-Plex Detection kit (Akoya Biosciences, NEL871001KT) according to the manufacturers' instructions. After deparaffinization, slides were subjected to epitope retrieval with Epitope Retrieval solution 2 (Leica Biosystems, AR9640), incubation with primary and secondary antibodies (Opal polymer HRP mouse plus rabbit, Akoya Biosciences, NEL871001KT), and tyramide signal amplification with Opal fluorophores (Table S4). Primary and secondary antibodies were removed during sequential epitope retrieval steps. Subsequently, slides were counterstained with spectral DAPI and mounted with ProLong Glass Antifade Mountant (Invitrogen, P36984). Whole slide scanning was performed on a Vectra Polaris multispectral imaging system.

86 cases of OCCC were classified according to the percent of cancer cells expressing HIF-1α and CAFs expressing FAP-α. Areas to be analyzed were selected based upon extensive presence of both PAX8-positive cancer cells and α-SMA-positive CAFs, and ≧3 areas were chosen to calculate the average value of fraction of HIF-1α-positive cells in PAX8 positive cancer cells and FAP-α-positive cells in α-SMA-positive CAFs. Samples with high level (>10%) or low level (<10%) of HIF-1α-positive fraction of cancer cells were categorized as HIF-1α high or HIF-1α low, respectively. Samples with high level (>80%) or low level (<80%) of FAP-α-positive fraction of CAFs were categorized as FAP-α high or FAP-α low, respectively.

QUANTIFICATION AND STATISTICAL ANALYSIS

Processing of snRNA-seq data

The gene count matrices were analyzed by Seurat software v3.2.2 running on R v3.6.0. The following cells were removed from the dataset: cells with >1% mitochondrial gene counts; cells with >6,000 unique featureCounts; and cells with <400 unique featureCounts. The gene-barcode matrix of the filtered cells was normalized using 'LogNormalize'. The top 2,000 variable genes were then identified using the 'vst' method in the Seurat FindVariableFeatures function. All cells from ten OCCC samples were integrated using the FindIntegrationAnchors and the IntegrateData functions of Seurat. After filtering of cells and data integration, a total of 62,673 cells were subjected to scaling using the Seurat ScaleData function. Subsequently, the scaled data were analyzed by PCA using the Seurat RunPCA function, with npcs = 30 parameters. UMAP plots were generated by the Seurat RunUMAP function, with dims = 1:30.

Annotation of cell populations in OCCC

To stratify cell populations using the integrated snRNA-seq data, low-resolution clustering was performed using the FindClusters function, with a resolution of 0.2. To annotate the five classified cell populations, specific marker genes were used to identify cell

populations corresponding to epithelial cell and non-tumor cell populations (Figure S1C). Annotation of these cell populations was confirmed by examining expression of various marker genes (Figure S1D).[52,53]

Copy number inference from sequencing data

InferCNV (https://github.com/broadinstitute/inferCNV) was used to analyze large-scale chromosome copy number alterations based on the single-cell sequencing data. The InferCNV pattern in each chromosome was examined in epithelial cells, using non-tumor cells (CAFs and endothelial cells) as a reference.

Enrichment analysis

To perform ssGSEA of cancer subpopulations, measurement of the signature scores for HALLMARK gene sets[54] expressed by each cancer subpopulation was based upon ssGSEA of the single-nucleus RNA-seq data. ssGSEA was performed using escape (v1.8.0, http://www.bioconductor.org/packages/release/bioc/vignettes/escape/inst/doc/vignette.html) running on R v4.2.1. To perform GO enrichment analyses, differentially expressed genes (DEGs) were selected using the FindAllMarkers function in Seurat. Subsequently, clusterProfiler[55] (v4.2.2) used the DEGs in each subpopulation to identify the top 10 most significant GO terms in biological processes (BP) categories.

Quantification of transcription factor activity

The activity of major transcription factors in each cell was inferred by VIPER (Virtual Inference of Protein-activity by Enriched Regulon analysis) v1.30.0 running on R v4.2.1. Transcription factor-target interactions classified as confidence level A (DoRothEA v1.6.0[45]) were used exclusively to calculate VIPER scores. VIPER scores were visualized in violin plots and heatmaps. Transcription factor-target interactions of the Cancer #2 cluster (shown in Figure S2D) were depicted by the igraph package in R.

Prognosis analysis

The top 20 DEGs that were selected using the FindAllMarkers function of Seurat were defined as signature genes for each cancer subpopulation. Surgical specimens of thirty advanced stage OCCC (Stages II-IV) were subjected to bulk RNA-seq analyses, and the patients were classified into two groups based upon average expression of the signature genes. Kaplan–Meier analysis was performed using the 'Survival' package in R to evaluate the prognostic value of cancer cell clusters. *p* values for overall survival and progression-free survival were evaluated using a stratified log rank test.

Ligand-receptor interaction analysis

Ligand-receptor interaction analysis based on snRNA-seq data was performed by NicheNet.[24] Ligands and receptors were selected from the DEGs of each cell population using the FindAllMarkers function in Seurat. The selected ligands form the Cancer #2 subpopulation were used to identify paired receptors from the DEGs of non-tumor cells based on the NicheNet ligand-receptor network. The Seurat AverageExpression function was used to visualize average expression of the ligands and receptors of each population in the heatmap. Subsequently, the interaction potential between the selected ligand-receptor pairs was estimated using NicheNet weighted integrated networks.

Spatial transcriptomics data processing

The Visium spot-gene expression matrices and spatial information of spatial transcriptomics data were imported into Seurat v3.2.0 for downstream analysis. The Sctransform function of Seurat was used to normalize the UMI count in each spot.[56] The object was run through PCA using the Seurat RunPCA function, with npcs = 20 parameters, and UMAP plots were generated by the Seurat RunUMAP function, with dims = 1:20. Clustering of the Visium spots was performed using the FindClusters function with resolution = 20.

Integration of snRNA-seq and spatial transcriptomics data

An anchor-based integration method in Seurat v3.2.0[18] was used to integrate snRNA-seq and Visium data. Transfer anchors were detected using the Seurat FindTransferAnchors function, setting the combined snRNA-seq datasets as a reference and one of the Visium datasets as a query. Following integration, the cluster labels of snRNA-seq datasets were transferred to the spatial dataset using the Seurat TransferData function, thereby providing a prediction score for each snRNA-seq cluster per spot.

Processing of scRNA-seq data

The gene count matrices were imported to Seurat software v3.2.2 running on R v3.6.0. The following cells were removed from the dataset: cells with >10% mitochondrial gene counts; cells with >6,000 unique featureCounts; and cells with <200 unique featureCounts. The filtered gene-barcode matrix was normalized using 'LogNormalize' in Seurat. Subsequently, the top 2,000 variable genes were then identified using the 'vst' method in the Seurat FindVariableFeatures function. Data obtained from co-cultured and monocultured cells were merged using the Seurat merge function. After filtering and merging, a total of 8,208 cells were processed for the following analysis: The merged object was scaled via the Seurat ScaleData function and run through PCA using

the Seurat RunPCA function, with npcs = 30. UMAP plots were generated by the Seurat RunUMAP function, with dims = 1:30. ssGSEA and VIPER analyses were performed as described above.

Image analysis of multiplexed immunofluorescence

QuPath[48] (version 0.2.1) was used to measure immunofluorescence intensity in tumor and non-tumor cells. After loading whole images, cells were segmented using StarDist,[57,58] and the fluorescence intensity of each cell was measured. Subsequently, cancer cells and CAFs were identified based on expression of PAX8 and α-SMA, respectively. An identical threshold intensity for immunofluorescence signals was applied for all samples. The centroid distances between α-SMA (+) cells and PAX8 (+)/HIF-1α (+) cells were estimated using the "Detect centroid distance 2D" command. After annotation of each cell, data were exported into CytoMAP[50] (version 1.4.21) for nearest neighbor analysis.

Statistical analyses of multi-color immunostaining data

Kaplan–Meier analysis was performed by 'Survival' package in R to evaluate the prognostic value of HIF-1α-expressing cancer cell and FAP-α-expressing CAFs. *p*-values of overall survival and progression free survival were evaluated by performing a stratified log rank test. Univariate and multivariate survival analysis was carried out using the Cox proportional hazards regression model. The average distance from FAP-α-positive cell to nearest HIF-1α -positive/negative cell was calculated as described above.

Cell Reports Medicine, Volume *5*

Supplemental information

Targeting PDGF signaling of cancer-associated fibroblasts blocks feedback activation of HIF-1α and tumor progression of clear cell ovarian cancer

Yutaro Mori, Yoshie Okimoto, Hiroaki Sakai, Yusuke Kanda, Hirokazu Ohata, Daisuke Shiokawa, Mikiko Suzuki, Hiroshi Yoshida, Haruka Ueda, Tomoyuki Sekizuka, Ryo Tamura, Kaoru Yamawaki, Tatsuya Ishiguro, Raul Nicolas Mateos, Yuichi Shiraishi, Yasushi Yatabe, Akinobu Hamada, Kosuke Yoshihara, Takayuki Enomoto, and Koji Okamoto

Mori et al. Figure S1

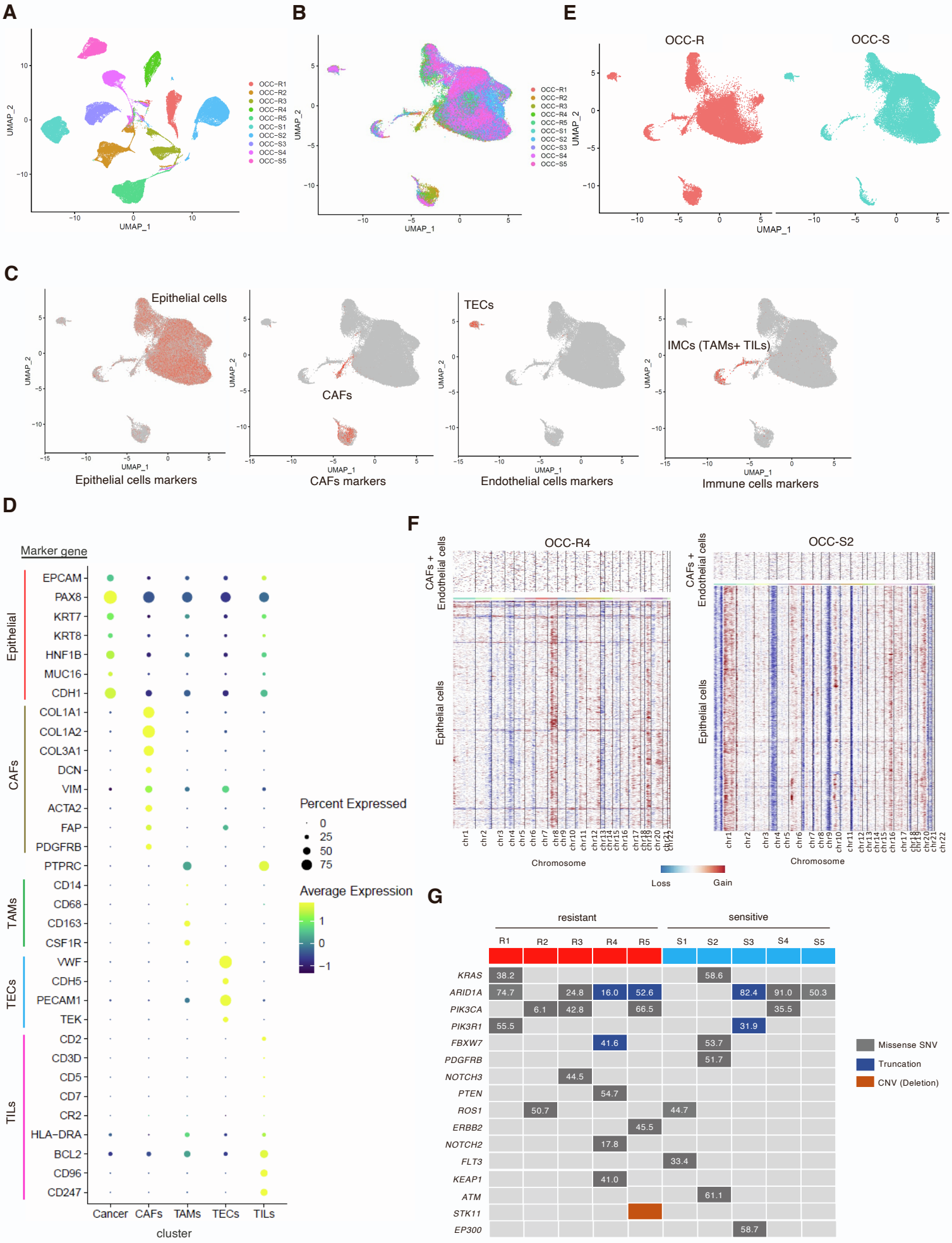

Figure S1. Identification of cancer subpopulations associated with chemoresistance of OCCC. Related to Figure 1.

(A) UMAP plot of chemoresistant (OCC-R) and chemosensitive (OCC-S) OCCC cells that passed quality control and were color-labeled according to the indicated clinical cases.

(B) Original snRNA-seq data from OCCC cases were subjected to an anchoring procedure, and the integrated datasets were used to generate the UMAP plot.

(C) Feature plots on the integrated UMAP showing expression of marker genes of each population. Expression of representative markers of epithelial cells (*EPCAM*, *PAX8*, *KRT7*), CAFs (*COL1A1*, *COL1A2*, *DCN*, *VIM*), endothelial cells (TECs) (*VWF*, *CDH5*, *PECAM1*), and immune cells (IMCs (TAMs +TILs)) (*PTPRC*) are shown.

(D) Dot plots of expression of marker genes in the indicated cell types.

(E) UMAP of OCCC cells, color-labeled according to chemoresistant and chemosensitive cases.

(F) Heatmap of copy-number alterations inferred from snRNA-seq data (OCC-R4 and OCC-S2) based on the average relative expression of 100 genes within sliding windows. Rows in the upper and lower panels correspond to non-tumor cells (CAFs + endothelial cells) and epithelial cells, respectively. Data from non-tumor cells were used as a reference.

(G) Genomic alterations in OCCC tumors. Colors indicate the type of genomic alteration. The numbers in the box represent the variance rate of each gene mutation (%).

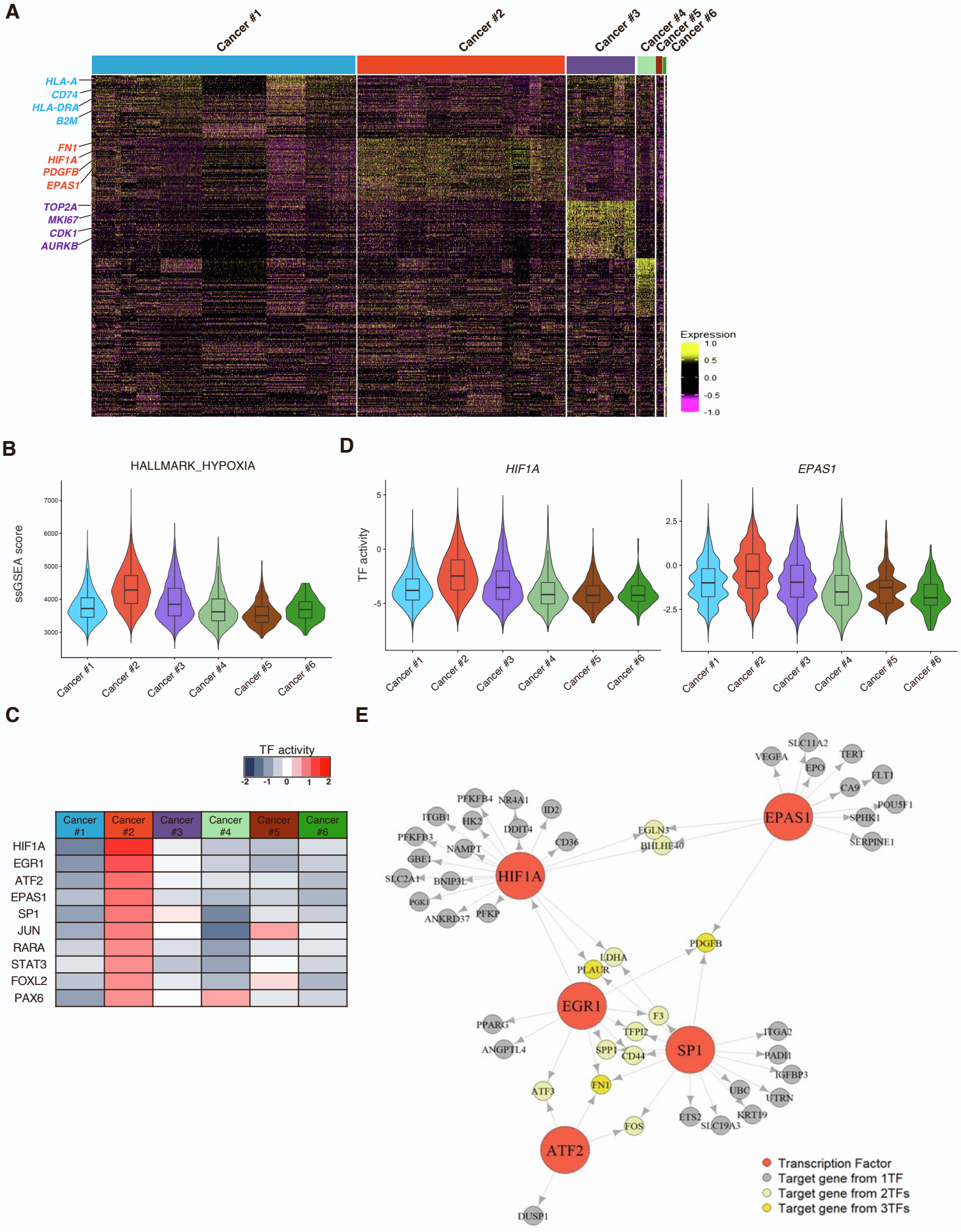
A
Cancer #1
Cancer #2
Cancer #3
Cancer #4
Cancer #5
Cancer #6
HLA-A
CD74
HLA-DRA
B2M
FN1
HIF1A
PDGFB
EPAS1
TOP2A
MKI67
CDK1
AURKB
Expression
1.0
0.5
0.0
-0.5
-1.0
B
HALLMARK_HYPOXIA
ssGSEA score
7000
6000
5000
4000
3000
Cancer #1
Cancer #2
Cancer #3
Cancer #4
Cancer #5
Cancer #6
D
HIF1A
EPAS1
TF activity
5
0
-5
2.5
0.0
-2.5
C
TF activity
-2
-1
0
1
2
Cancer #1
Cancer #2
Cancer #3
Cancer #4
Cancer #5
Cancer #6
HIF1A
EGR1
ATF2
EPAS1
SP1
JUN
RARA
STAT3
FOXL2
PAX6
E
SLC11A2
VEGFA
TERT
EPO
FLT1
CA9
POU5F1
SPHK1
SERPINE1
EPAS1
PFKFB4
NR4A1
ID2
ITGB1
HK2
DDIT4
PFKFB3
NAMPT
CD36
GBE1
SLC2A1
BNIP3L
HIF1A
PGK1
ANKRD37
PFKP
EGLN3
BHLHE40
PDGFB
LDHA
PLAUR
EGR1
PPARG
ANGPTL4
F3
TFPI2
SPP1
CD44
SP1
ITGA2
PADI1
IGFBP3
ATF3
FN1
UBC
UTRN
ETS2
KRT19
SLC19A3
FOS
ATF2
DUSP1
Transcription Factor
Target gene from 1TF
Target gene from 2TFs
Target gene from 3TFs

Figure S2. Chemoresistant population of OCCC is associated with HIF activation and poor prognosis. Related to Figure 2.

(A) Heatmap of top-ranking genes in each subpopulation. Representative genes in the Cancer #1–3 subpopulations are shown.

(B) Violin plots of hallmark-hypoxia signature scores for the indicated cancer subpopulations.

(C) Heatmap of transcription factor (TF) activity, as inferred by the VIPER algorism, in the indicated cancer subpopulations. The 10 top-ranked TF genes in the Cancer #2 subpopulation are shown.

(D) Violin plots of HIF1A and EPAS1(HIF2A) TF activity in the indicated cancer subpopulations.

(E) Schematic representation of a regulatory network of TFs and their downstream genes that are activated in the Cancer #2 subpopulation. TFs activated in the Cancer #2 subpopulation are denoted by large red circles, and their target genes (listed in DoRothEA) are denoted by small circles. Target genes regulated by one, two, or three TFs are shown in gray, cream-yellow, or orange, respectively.

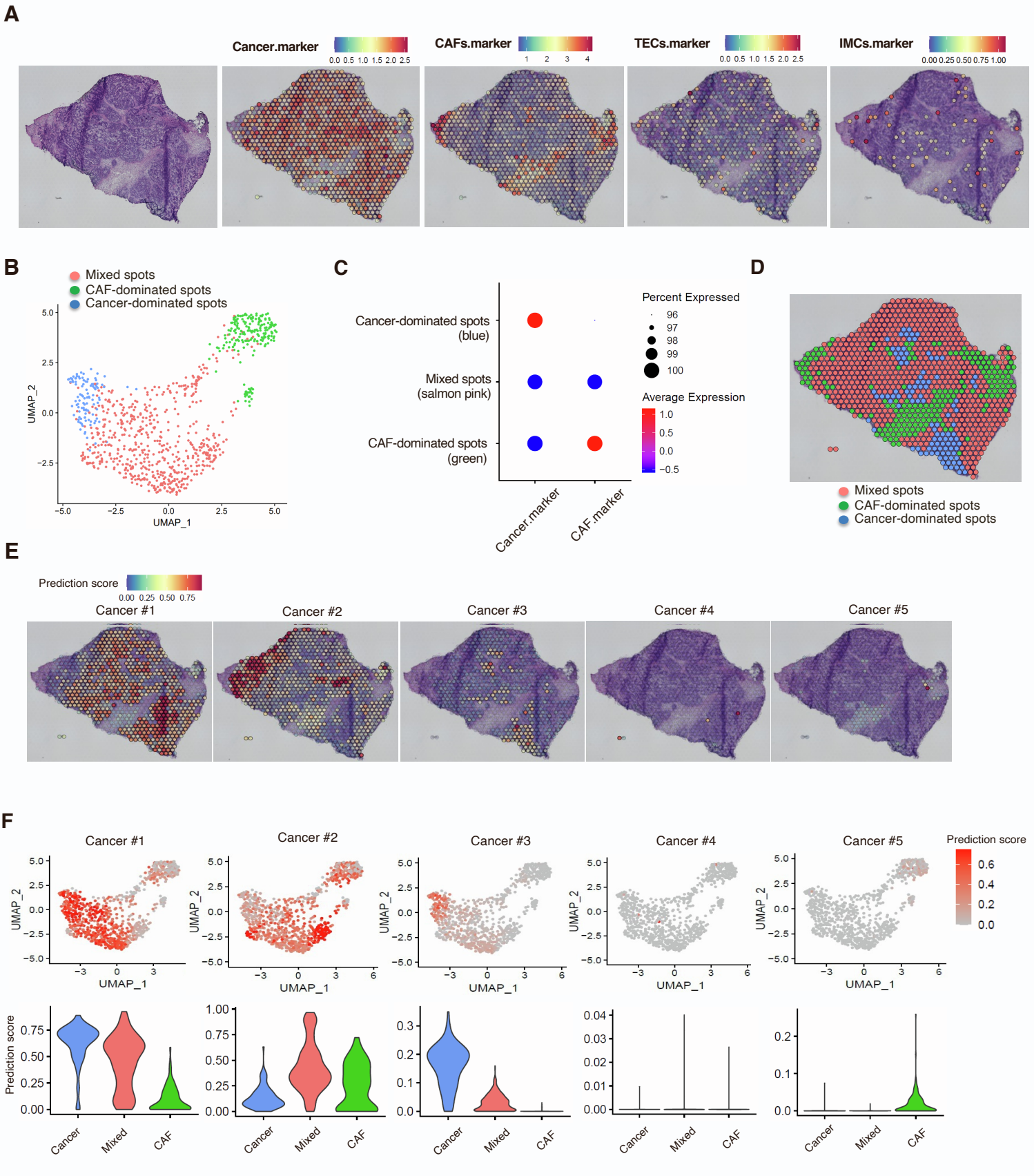
A
Cancer.marker
0.0 0.5 1.0 1.5 2.0 2.5
CAFs.marker
1 2 3 4
TECs.marker
0.0 0.5 1.0 1.5 2.0 2.5
IMCs.marker
0.00 0.25 0.50 0.75 1.00
B
Mixed spots
CAF-dominated spots
Cancer-dominated spots
UMAP_2
UMAP_1
C
Cancer-dominated spots (blue)
Mixed spots (salmon pink)
CAF-dominated spots (green)
Cancer.marker
CAF.marker
Percent Expressed
96
97
98
99
100
Average Expression
1.0
0.5
0.0
−0.5
D
Mixed spots
CAF-dominated spots
Cancer-dominated spots
E
Prediction score
0.00 0.25 0.50 0.75
Cancer #1
Cancer #2
Cancer #3
Cancer #4
Cancer #5
F
Cancer #1
Cancer #2
Cancer #3
Cancer #4
Cancer #5
Prediction score
0.6
0.4
0.2
0.0
UMAP_2
UMAP_1
Prediction score
Cancer
Mixed
CAF

Figure S3. Chemoresistant cells are localized in CAF-populated areas of OCCC. Related to Figure 3.

(A) (far left) H&E staining of OCC-S3 tissue sections. (right) ST spots on H&E-stained sections were overlaid with spatial feature plots of ovarian cancer cell markers (*EPCAM*, *PAX8*, *KRT7*), CAF markers (*COL1A1*, *COL1A2*, *DCN*, *VIM*), endothelial cell (TEC) markers (*VWF*, *CDH5*, *PECAM1*), or an immune cell (IMC) marker (*PTPRC*).

(B) UMAP plots of the ST spots shown in a. ST spots were classified into three clusters by unsupervised clustering, and denoted by different colors.

(C) Dot plots showing average expression of CAF markers and ovarian cancer cell markers in the indicated clusters. Three clusters shown in B were designated as cancer-dominated spots, CAF-dominated spots, and Mixed spots, based upon marker expression.

(D) Spatial presentation of the three cluster in OCC-S3 tissue sections. Tissue localization of the clustered ST spots was visualized and denoted by the indicated colors.

(E) Spatial feature plots of the prediction scores for the indicated cancer subpopulations (Cancer #1–5) in OCC-S3 tissue sections.

(F) Top: UMAP feature plots of ST spots of OCC-S3. Prediction scores for the indicated cancer subpopulations are shown in red. Bottom: Violin plots of the prediction scores for cancer subpopulations shown in the top columns. ST spots were classified into three groups as shown in d, and prediction scores for each group are presented.

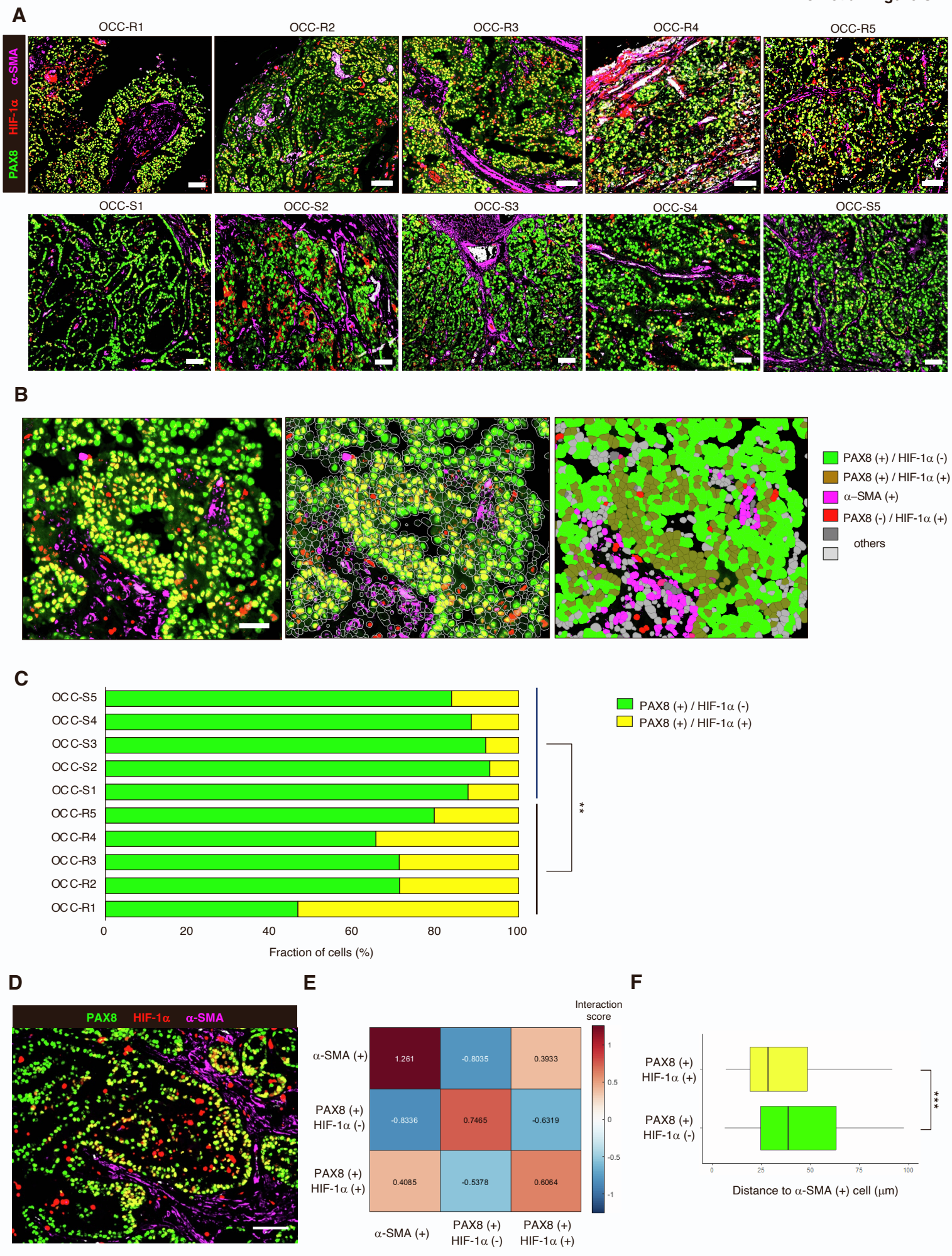
A
OCC-R1
OCC-R2
OCC-R3
OCC-R4
OCC-R5
PAX8
HIF-1α
α-SMA
OCC-S1
OCC-S2
OCC-S3
OCC-S4
OCC-S5
B
PAX8 (+) / HIF-1α (-)
PAX8 (+) / HIF-1α (+)
α–SMA (+)
PAX8 (-) / HIF-1α (+)
others
C
OCC-S5
OCC-S4
OCC-S3
OCC-S2
OCC-S1
OCC-R5
OCC-R4
OCC-R3
OCC-R2
OCC-R1
0
20
40
60
80
100
Fraction of cells (%)
**
PAX8 (+) / HIF-1α (-)
PAX8 (+) / HIF-1α (+)
D
PAX8
HIF-1α
α-SMA
E
Interaction score
α-SMA (+)
PAX8 (+) HIF-1α (-)
PAX8 (+) HIF-1α (+)
1.261
-0.8035
0.3933
-0.8336
0.7465
-0.6319
0.4085
-0.5378
0.6064
1
0.5
0
-0.5
-1
α-SMA (+)
PAX8 (+) HIF-1α (-)
PAX8 (+) HIF-1α (+)
F
PAX8 (+) HIF-1α (+)
PAX8 (+) HIF-1α (-)
***
0
25
50
75
100
Distance to α-SMA (+) cell (μm)

Figure S4. HIF-1α-expressing cancer cells reside near CAFs in chemoresistant OCCC. Related to Figure 3.

(A) Representative images of co-immunostaining of chemosensitive and chemoresistant tumors with HIF-1α (Red), PAX8 (Green), and α-SMA (Pink). Scale bar, 100 μm.

(B) Segmented cells were annotated by the image processing algorithm in QuPath. (Left) A representative image of coimmunostaining of chemoresistant tumor (OCC-R2). (Middle) Cell segmentation. (Right) Annotation of segmented cells based upon immunostaining.

(C) Percentage of HIF-1α(+) cancer cells (calculated from whole-slide images of tumor sections). $^{**}p < 0.01$.

(D) Representative magnified images of HIF-1α(+) cancer cells near to α-SMA (+) CAF in a chemoresistant tumor (OCC-R2). Scale bar, 100 mm.

(E) Nearest neighbor analysis of the image shown in D.

(F) Box plot of average distance from PAX8(+)/HIF-1α(+) cells or PAX8(+)/HIF-1α(-) cells to the nearest α-SMA(+) cells, calculated from the image shown in D. *P* values were determined by Student's t test. Statistically significant differences are indicated: $^{***}p < 0.001$.

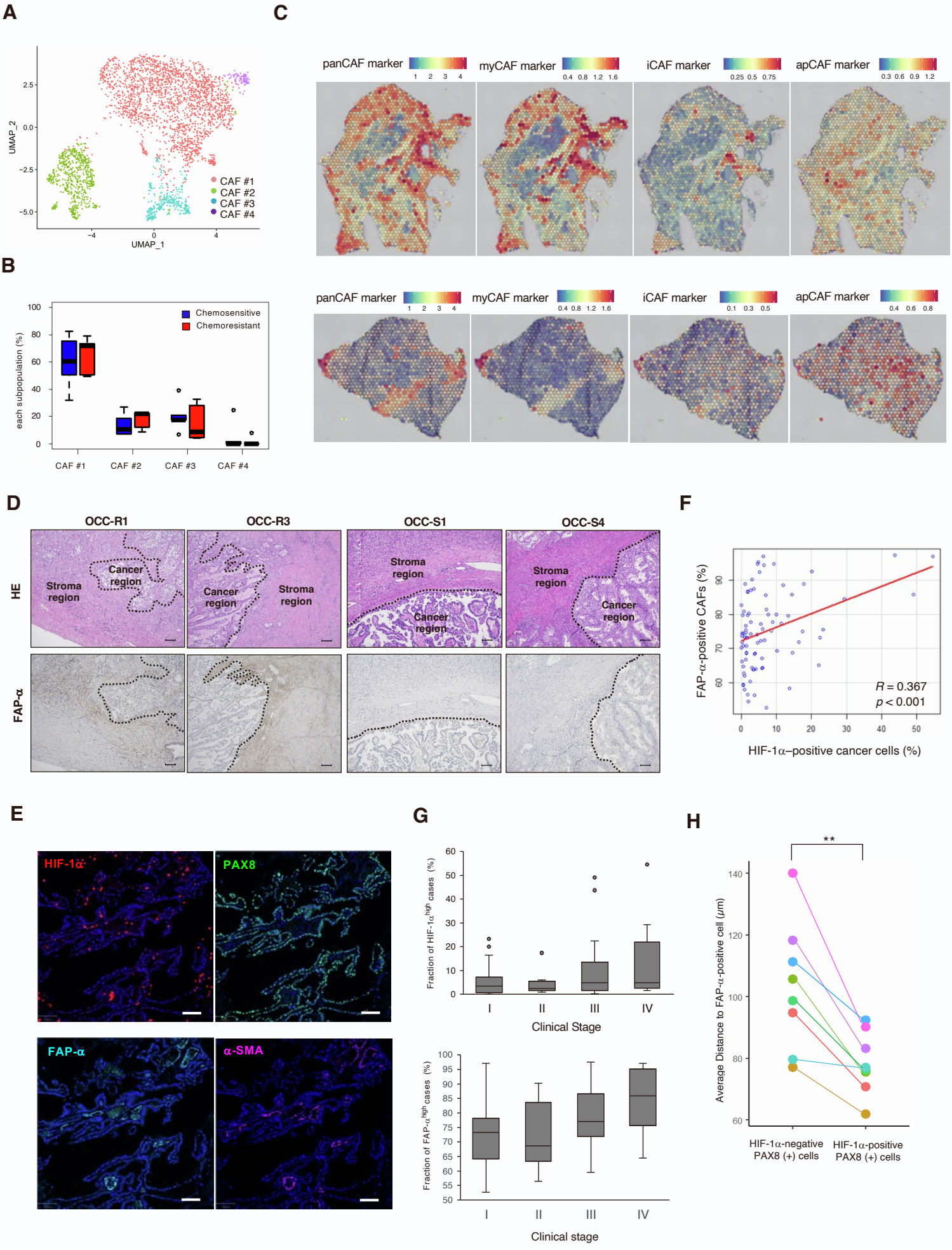
A
UMAP_2
UMAP_1
CAF #1
CAF #2
CAF #3
CAF #4
B
each subpopulation (%)
Chemosensitive
Chemoresistant
CAF #1
CAF #2
CAF #3
CAF #4
C
panCAF marker
myCAF marker
iCAF marker
apCAF marker
D
OCC-R1
OCC-R3
OCC-S1
OCC-S4
HE
FAP-α
Stroma region
Cancer region
E
HIF-1α
PAX8
FAP-α
α-SMA
F
FAP-α-positive CAFs (%)
HIF-1α–positive cancer cells (%)
R = 0.367
p < 0.001
G
Fraction of HIF-1α high cases (%)
Fraction of FAP-α high cases (%)
Clinical Stage
Clinical stage
I
II
III
IV
H
Average Distance to FAP-α-positive cell (μm)
**
HIF-1α-negative PAX8 (+) cells
HIF-1α-positive PAX8 (+) cells

Figure S5. CAFs in chemoresistant tumors are associated with myofibroblastic phenotype. Related to Figure 4.

(A) UMAP plot of the OCCC CAFs shown in Fig. 5a, color-coded into four subpopulations (CAF #1–4) by unsupervised clustering.

(B) Box plots of percentage of the indicated CAF subpopulations from the chemoresistant and chemosensitive tumors shown in A.

(C) Spatial feature plots of panCAF markers, myCAF markers, iCAF markers, and apCAF markers in OCC-R2 (top) and OCC-S3 (bottom) tissue sections.

(D) H&E images and immunostaining with FAP-α in indicated chemoresistant and chemosensitive tumors. Dotted lines depict the boundary between the tumor and the stroma regions. Scale bar: 100 μm.

(E) Representative immunostaining with HIF-1α, PAX8, α-SMA, or FAP-α by Vectra Polaris multi-color imaging system. Scale bar: 100 μm.

(F) Fraction of HIF-1α-positive cancer cells and FAP-α-positive CAFs in 86 cases of OCCC. Correlation between the percentage of HIF-1α-positive cancer cells and FAP-α-positive CAFs was determined by calculating Pearson's correlation coefficient.

(G) Percentage of HIF-1α^{high} and FAP-α^{high} cases in each stage. Stage I (n=45), Stage II (n=8), Stage III (n=24), and Stage IV (n=9). Top and bottom end of the boxes represent 25% and 75% percentile, respectively, and horizontal bars in the box indicate median values.

(H) Dot plot showing average distances from FAP-α-positive cell to nearest HIF-1α-positive or HIF-1α-negative cell. Multi-color fluorescent images of HIF-1α^{high}/FAP-α^{high} samples (n=8) were used to calculate the average distances as described in the Method section. The same samples share identical color. *p*-values were determined by student t-test. ** $p < 0.01$.

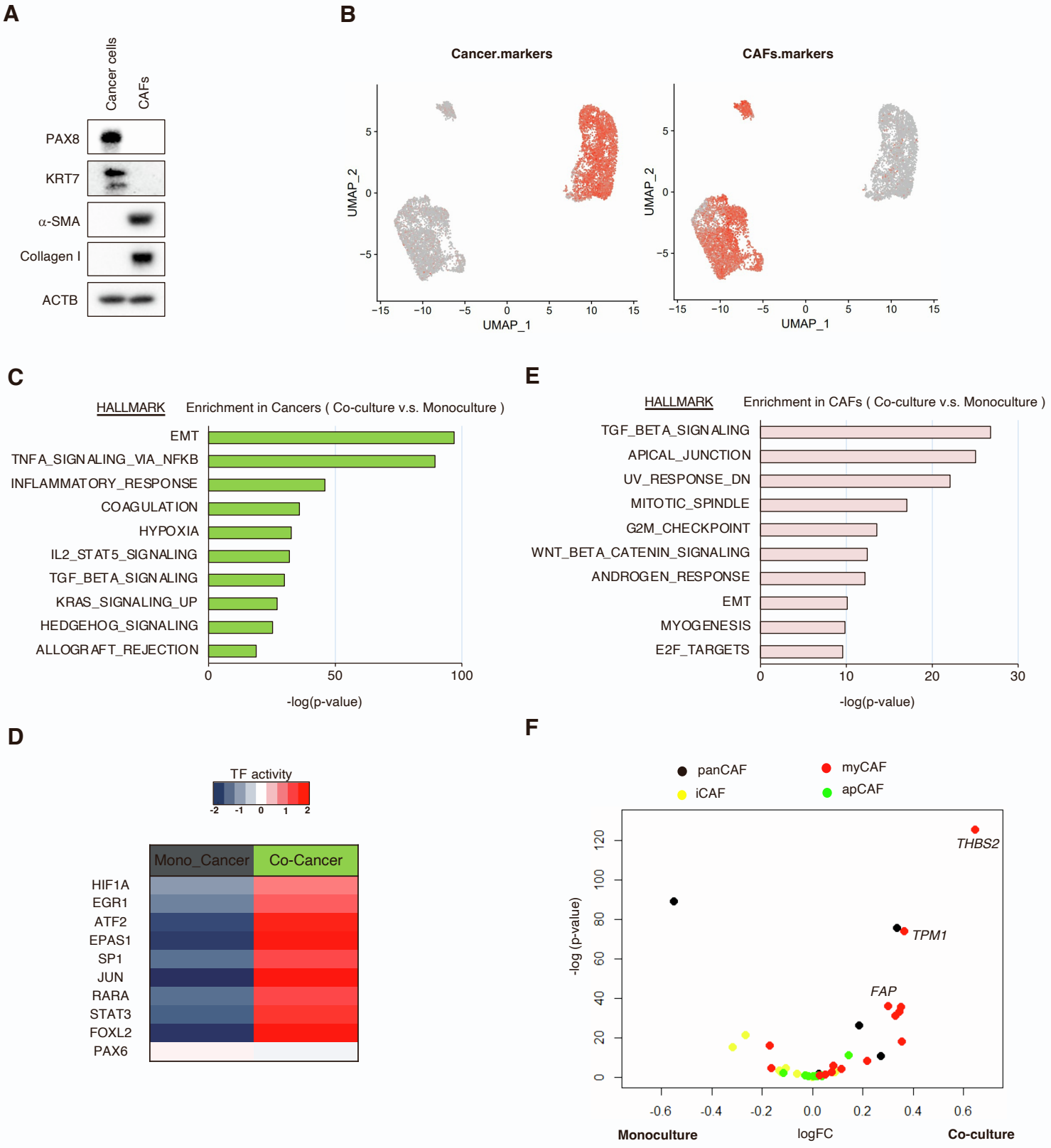
A
Cancer cells
CAFs
PAX8
KRT7
α-SMA
Collagen I
ACTB
B
Cancer.markers
CAFs.markers
UMAP_2
UMAP_1
C
HALLMARK Enrichment in Cancers (Co-culture v.s. Monoculture)
EMT
TNFA_SIGNALING_VIA_NFKB
INFLAMMATORY_RESPONSE
COAGULATION
HYPOXIA
IL2_STAT5_SIGNALING
TGF_BETA_SIGNALING
KRAS_SIGNALING_UP
HEDGEHOG_SIGNALING
ALLOGRAFT_REJECTION
-log(p-value)
E
HALLMARK Enrichment in CAFs (Co-culture v.s. Monoculture)
TGF_BETA_SIGNALING
APICAL_JUNCTION
UV_RESPONSE_DN
MITOTIC_SPINDLE
G2M_CHECKPOINT
WNT_BETA_CATENIN_SIGNALING
ANDROGEN_RESPONSE
EMT
MYOGENESIS
E2F_TARGETS
-log(p-value)
D
TF activity
Mono_Cancer
Co-Cancer
HIF1A
EGR1
ATF2
EPAS1
SP1
JUN
RARA
STAT3
FOXL2
PAX6
F
panCAF
myCAF
iCAF
apCAF
THBS2
TPM1
FAP
-log (p-value)
Monoculture
logFC
Co-culture

Figure S6. Co-cultivation of CAFs and chemoresistant OCCC cells *in vitro* recapitulates the chemoresistant niche. Related to Figure 5.

(A) Western blot analysis of established cancer cells (OVN-48) and CAFs.

(B) UMAP feature plots of cancer & CAF markers in the cultivated cells shown in Figure 6G.

(C) Bar chart showing enrichment of specific biological pathways in cancer cells in the presence of CAFs. Enrichment of a pathway is calculated by comparing the average ssGSEA values of HALLMARK gene sets in cancer cells under co-culture and monoculture conditions. *P*-values of the top 10 terms enriched in cancer cells co-cultured with CAFs are shown.

(D) Heatmap of normalized TF activity in cancer cells under monoculture and co-culture conditions. The VIPER scores for the Top 10 TF genes activated in the Cancer #2 subpopulation (Figure S2C) are shown. There was no detectable expression of PAX6 in cancer cells, and its VIPER score was not calculated.

(E) Bar chart showing enrichment of specific biological pathways in CAFs in the presence of cancer cells. Enrichment of a pathway is calculated by comparing the average ssGSEA values of HALLMARK gene sets in CAFs under co-culture and monoculture conditions. *P*-values for the top 10 terms enriched in CAFs under co-culture conditions are shown.

(F) Volcano plots showing preferential induction of myCAF signature genes in CAFs co-cultured with cancer cells. The average expression values for the CAF signature genes (shown in Figure 5E) in CAFs under monoculture and co-culture conditions were calculated, and relative ratios are shown. The horizontal and vertical axes represent $\log_{10}$ -fold changes and *p*-values, respectively. Red dots: myCAF signature genes; Yellow dots: iCAF signature genes; Green dots: apCAF signature genes; Black dots: panCAF signature genes. A list of signature genes is presented in Table S3. *P*-values were determined by Student's t test.

A

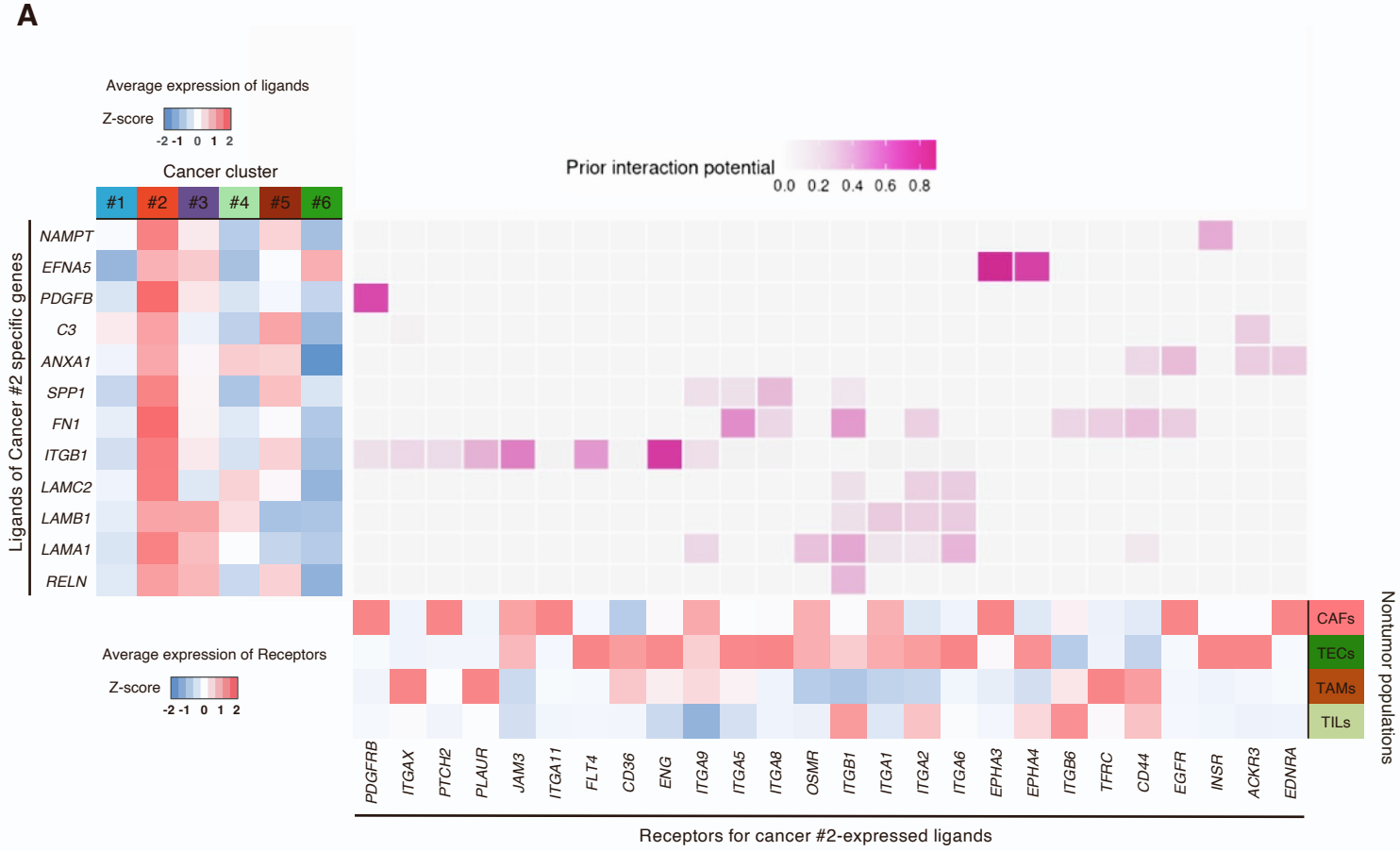
Average expression of ligands
Z-score
-2 -1 0 1 2
Cancer cluster
#1 #2 #3 #4 #5 #6
Ligands of Cancer #2 specific genes
NAMPT
EFNA5
PDGFB
C3
ANXA1
SPP1
FN1
ITGB1
LAMC2
LAMB1
LAMA1
RELN
Prior interaction potential
0.0 0.2 0.4 0.6 0.8
Average expression of Receptors
Z-score
-2 -1 0 1 2
CAFs
TECs
TAMs
TILs
Nontumor populations
PDGFRB
ITGAX
PTCH2
PLAUR
JAM3
ITGA11
FLT4
CD36
ENG
ITGA9
ITGA5
ITGA8
OSMR
ITGB1
ITGA1
ITGA2
ITGA6
EPHA3
EPHA4
ITGB6
TFRC
CD44
EGFR
INSR
ACKR3
EDNRA
Receptors for cancer #2-expressed ligands

B

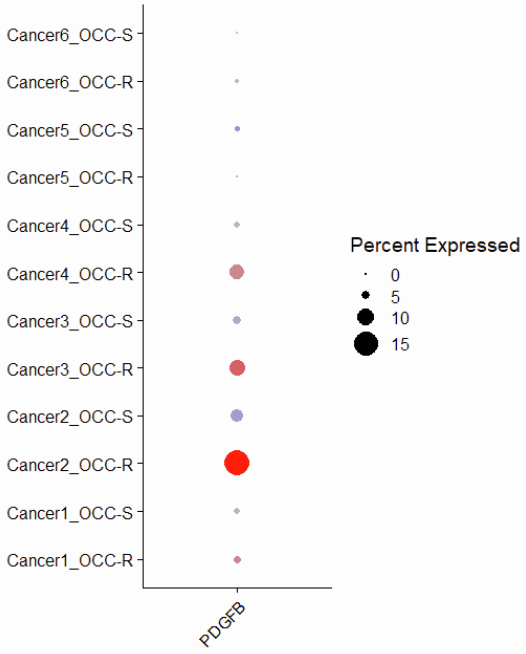
Cancer6_OCC-S
Cancer6_OCC-R
Cancer5_OCC-S
Cancer5_OCC-R
Cancer4_OCC-S
Cancer4_OCC-R
Cancer3_OCC-S
Cancer3_OCC-R
Cancer2_OCC-S
Cancer2_OCC-R
Cancer1_OCC-S
Cancer1_OCC-R
PDGFB
Percent Expressed
0
5
10
15

C

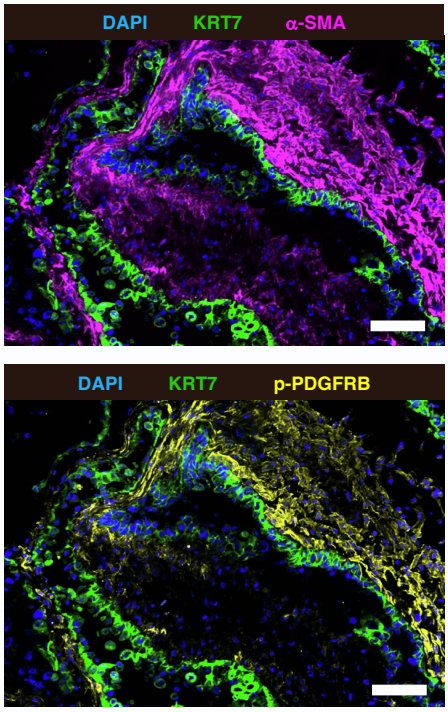
DAPI KRT7 α-SMA
DAPI KRT7 p-PDGFRB

Figure S7. CAF activation by cancer-derived PDGF mediates chemoresistance and HIF-1a expression of cancer cells. Related to Figure 6.

(A) Prediction of possible interactions between Cancer #2-expressed ligands and CAF-expressed receptors by using NicheNet. (Left matrix) heatmap showing expression of top-ranking ligands that are preferentially expressed in the Cancer #2 subpopulation. (Bottom matrix) heatmap showing corresponding receptors expressed in nontumor populations. (Middle) heatmap showing the potential interactions between ligand-receptor pairs between the Cancer #2 subpopulation and nontumor cells, which are based upon prior knowledge of signaling and gene regulatory networks predicted by NicheNet.

(B) Dot plots showing average expression of *PDGFB* in the indicated cancer subpopulations from the chemoresistant and chemosensitive cases

(C) Representative images of co-immunostaining of frozen sections of chemoresistant tumor (OCC-R3) with the indicated antibodies.

A

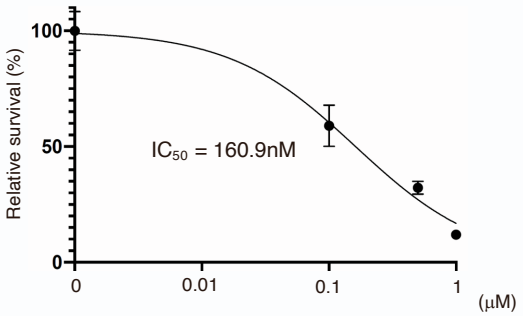
100
50
0
Relative survival (%)
IC50 = 160.9nM
0
0.01
0.1
1
(μM)

B

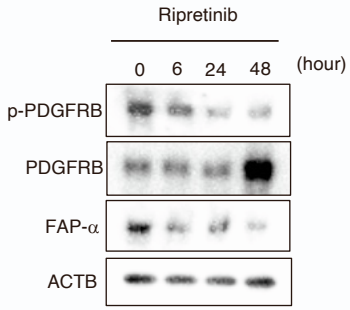
Ripretinib
0 6 24 48 (hour)
p-PDGFRB
PDGFRB
FAP-α
ACTB

C

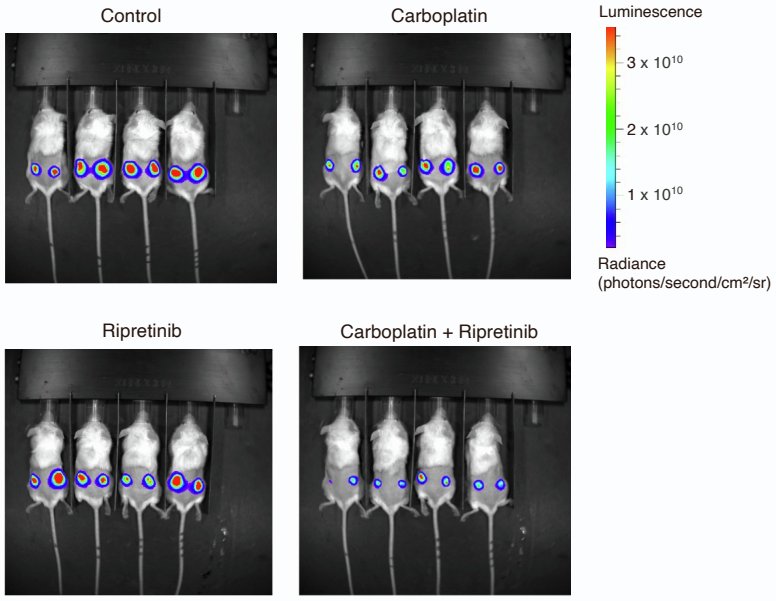
Control
Carboplatin
Luminescence
3 x 10^10
2 x 10^10
1 x 10^10
Radiance
(photons/second/cm²/sr)
Ripretinib
Carboplatin + Ripretinib

D

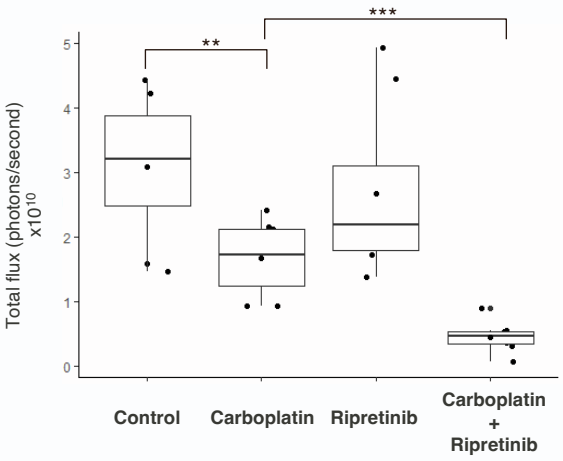
**
***
Total flux (photons/second)
x10^10
Control
Carboplatin
Ripretinib
Carboplatin
+
Ripretinib

E

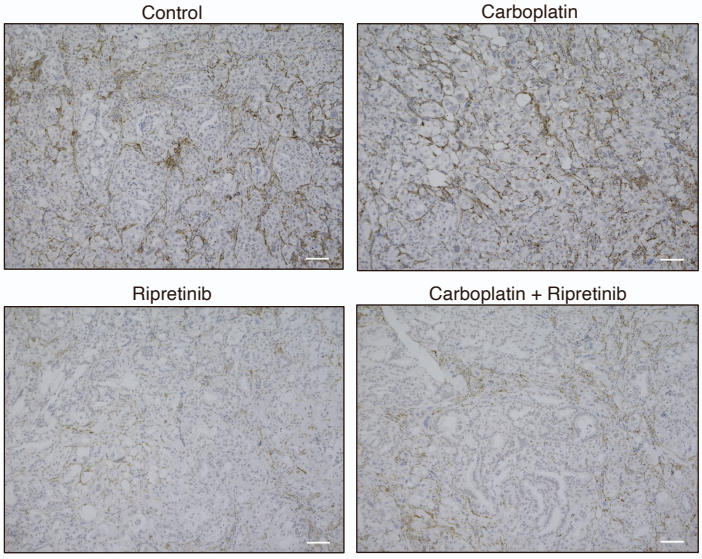
Control
Carboplatin
Ripretinib
Carboplatin + Ripretinib

F

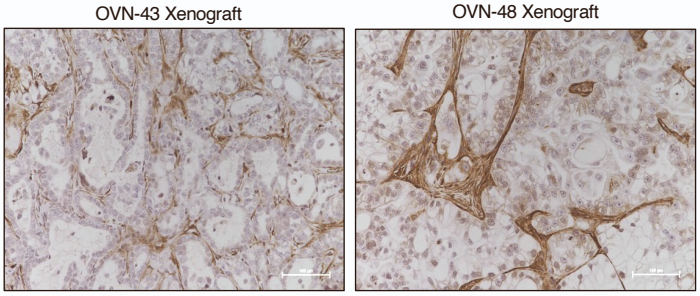
OVN-43 Xenograft
OVN-48 Xenograft

G

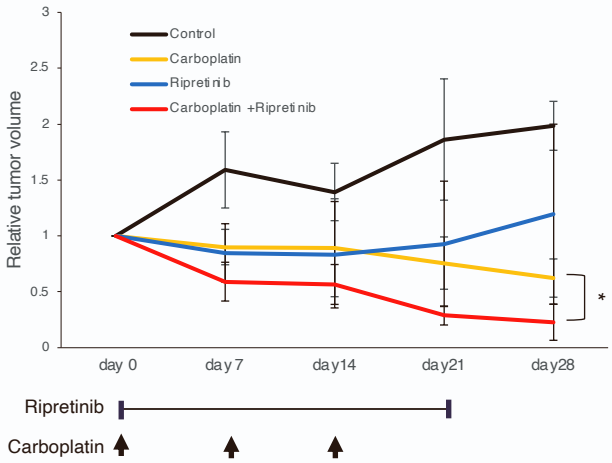
Control
Carboplatin
Ripretinib
Carboplatin +Ripretinib
Relative tumor volume
day 0
day 7
day14
day21
day28
*
Ripretinib
Carboplatin

Figure S8. CAF inhibition by Ripretinib in combination with Carboplatin blocks tumor growth of OCCC. Related to Figure 7.

(A) Dose-response curve of the CAFs treated with Ripretinib for 7 days.

(B) Western blot analyses of CAFs treated with 1μM Ripretinib for the indicated times.

(C) Bioluminescence images of luciferase activity in tumor xenografts treated as indicated (4 weeks after chemotherapy).

(D) Box plots of the luciferase activity shown in b, calculated by measuring total flux from the tumors. *P*-values were determined by Student's t test.

(E) Immunostaining of the tumor xenografts shown in C with an α-SMA antibody. Scale bars, 100 μm. Statistically significant differences are indicated: $^{**}p < 0.01$, $^{***}p < 0.001$.

(F) α-SMA Immunostaining of the xenografted tumors after injection of the indicated cancer spheroid cells alone. Scale bars: 100 μm.

(G) Xenografted tumors (OVN-43, 77 days after transplantation of cancer cells) were treated with the indicated combination of Carboplatin and/or Ripretinib, and tumor volumes were measured every week. The data are presented as mean ± SD (n=3). P-values were determined by Student's t test. $^{*}p < 0.05$.